arXiv:1704.05264v1 [physics.bio-ph] 18 Apr 2017

Universal entrainment mechanism governs contact times with motile cells

Arnold J. T. M. Mathijssen*
Department of Bioengineering, Stanford University, 443 Via Ortega, Stanford, CA 94305, United States

Raphaël Jeanneret† and Marco Polin‡
Physics Department, University of Warwick, Gibbet Hill Road, Coventry CV4 7AL, United Kingdom

(Dated: April 19, 2017)

Contact between particles and motile cells underpins a wide variety of biological processes, from nutrient capture and ligand binding, to grazing, viral infection and cell-cell communication. The window of opportunity for these interactions is ultimately determined by the physical mechanism that enables proximity and governs the contact time. Jeanneret et al. (Nat. Comm. 7: 12518, 2016) reported recently that for the biflagellate microalga *Chlamydomonas reinhardtii* contact with microparticles is controlled by events in which the object is entrained by the swimmer over large distances. However, neither the universality of this interaction mechanism nor its physical origins are currently understood. Here we show that particle entrainment is indeed a generic feature for microorganisms either pushed or pulled by flagella. By combining experiments, simulations and analytical modelling we reveal that entrainment length, and therefore contact time, can be understood within the framework of Taylor dispersion as a competition between advection by the no slip surface of the cell body and microparticle diffusion. The existence of an optimal tracer size is predicted theoretically, and observed experimentally for *C. reinhardtii*. Spatial organisation of flagella, swimming speed, swimmer and tracer size influence entrainment features and provide different trade-offs that may be tuned to optimise microbial interactions like predation and infection.

INTRODUCTION

The wide variety of microbial interactions is often deeply influenced by physics. Within biofilms, electric currents can coordinate cellular metabolic rates [1], while wrinkles draw nutrients by capillarity [2]. Microscopic flow fields [3–5] can lead to large scale collective motion [6–8] with enhanced drug resistance [9, 10], surprising rheological properties [11–13], and global features controllable by structured confinement [14–18]. When coupled with population-wide taxis, these flows result in macroscopic instabilities [19–21] which increase nutrient fluxes [22] and can provide, at the same time, unexpected new avenues for capture and manipulation of small objects [23].

For swimming microorganisms, many interactions hinge on close contact. These include fundamental processes like nutrient uptake [24–31], viral infection [32, 33], eukaryotic fertilisation [34], and grazing on both natural preys [30, 35–37] and the microplastics that currently litter our oceans [38, 39]. In all these cases, a finite contact time T will define the window of opportunity for the interaction with the microswimmer to take place. For a constant success rate per unit time Ω, the probability of a successful interaction is given by $p(T) = 1 - e^{-\Omega T}$ [37]. Large values of $p(T)$ will be favoured by long contact times, and will therefore depend on the physics that regulates proximity. Although the theoretical basis of contact times is still developing [40–42], it is reasonable to expect that a key role will be played by the properties of the near field, the region close to the cell body [30]. As already noted in this context by Purcell [43], the fluid layer close to a swimming microorganism is expected to be carried along by it. Small objects sufficiently close to a microswimmer are therefore entrained [44] and stay in close contact with it for the time required to escape the near-field region. Entrainment converts a temporal quantity, the contact time T, into a readily measurable spatial quantity, the entrainment length L. While recent studies have provided numerical support for particle entrainment by microorganisms [45–47], experimental evidence is limited to the microalga *Chlamydomonas reinhardtii* [48], and it is not clear whether or not this phenomenon is a general feature of microbial motility. At the same time, there are currently no theoretical predictions for the duration of these contact events, as a clear picture of the physics underlying entrainment is lacking [45–50].

Here we combine experimental, numerical and theoretical approaches to investigate particle entrainment by microorganisms. Results from the green microalgae *Chlamydomonas reinhardtii* and *Tetraselmis subcordiforms* -pulled by different numbers of anterior flagella- and the dinoflagellate *Oxyrrhis marina* -pushed by a posterior flagellum- demonstrate that entrainment is indeed a robust generic feature amongst swimming cells, largely independent of the propulsion strategy. Comparing experiments with theoretical results and simulations based on a realistic time-dependent swimmer model, we show that entrainment is a direct consequence of a no-slip cell surface, as recently suggested in [46], and that particle size affects its duration through a combination of advection and diffusion. The ensuing non-monotonic dependence reveals an optimal particle size for entrainment and is captured well by a simple model based on Taylor

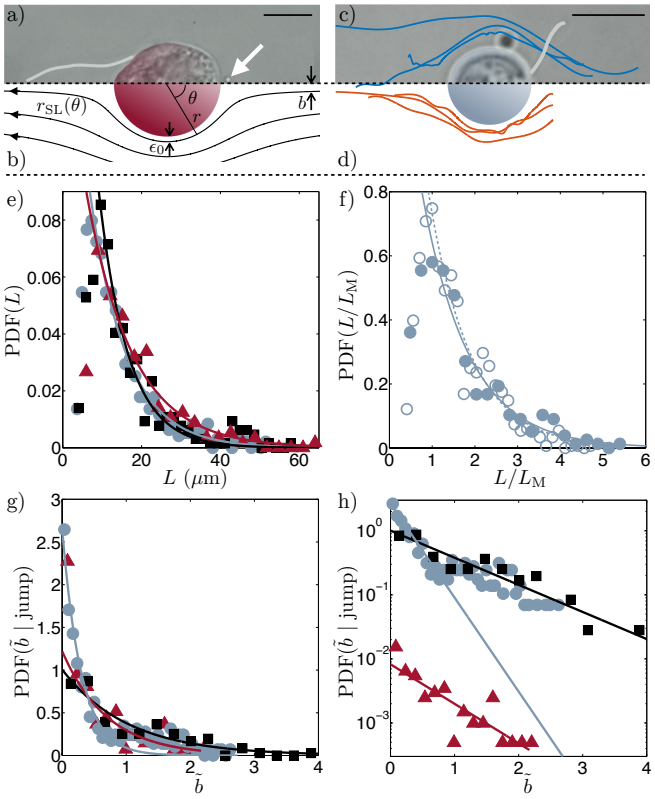

FIG. 1. a) Snapshot of typical particle entrainment events for OM. The colloid ($r_P = 0.5\ \mu$m) is shown with a white arrow. Scale bar: 10 μm. b) Diagram and approximated streamlines $r_{SL}(\theta) = r_S + b\sqrt{2/3}/\sin(\theta)$ of the swimmer-generated flow in its co-moving frame. c) (resp. d)) Typical experimental (resp. numerical) tracer trajectories in the frame of CR. Scale bar: 10 μm. e) PDF of entrainment length L obtained with tracers of radius $r_P = 0.5\ \mu$m for three different organisms: red triangles: OM; grey circles: CR; black squares: TS. Above a peak at value $L_M^{(S)}$, those are fitted by an exponential distribution with characteristic length scale $L_J^{(S)}$. f) Comparison of experimental (filled grey circles) and numerical (empty grey circles) jump lengths distributions using our outboard CR, for small impact parameters and normalised by L_M, the length at the maximum: $L_M^{(sim)} \approx 14.5\ \mu$m and $L_M^{(exp)} \approx 9.4\ \mu$m. g) Conditional PDF of the rescaled impact parameter $\tilde{b} = 2b/w$ given an entrainment event PDF($\tilde{b}$ | jump). Curves are fitted by exponential distributions with characteristic lengths: $\tilde{b}^{(TS)} = 1.0 \pm 0.3$, $\tilde{b}^{(CR)} = 0.30 \pm 0.05$ and $\tilde{b}^{(OM)} = 0.70 \pm 0.25$. Same color code as in e). h) Same data in a semi-log plot with the curve for OM (red triangles) shifted to highlight the two regimes in the distribution for CR (grey circles).

dispersion.

MATERIALS AND METHODS

We briefly summarise here our experimental and numerical methods, and refer the reader to the Supplementary Information (SI) for a detailed description of our procedures.

Experiments

As described in SI §1, *Chlamydomonas reinhardtii* wild type strain CC125 (CR), *Tetraselmis subcordiforms* CCAP 161/1A (TS) and *Oxyrrhis marina* CCAP 1133/5 (OM) were grown respectively in Tris-acetate-phosphate medium [51], Seawater Nutrient Broth and f/2 medium (with the alga *Nannochloropsis oculata* as food) at 21°C under periodic fluorescent illumination (12h/12h). Cultures were harvested in the exponential phase ($\sim 10^6$ cells/ml for CR and TS, $\sim 10^5$ cells/ml for OM), resuspended in fresh medium, and polystyrene microparticles (Polysciences) of the required radius ($r_P = 0.50 \pm 0.01\mu$m for TS and OM, $0.26 \pm 0.005 \leq r_P \leq 1.55 \pm 0.03\mu$m for CR) were added to a concentration $\lesssim 10^{-4}\%$ solids. The suspensions were then loaded into 26 μm-thick (CR and TS, 29 μm-thick for OM) and 5 mm-wide microfluidic chambers similar to the Hele-Shaw cells used in [48]. We automatically extracted candidate entrainment events from long-timescale tracking of colloidal particles, followed by visual inspection to filter out spurious events. The three species studied have similar prolate bodies (length $l = 10.1, 13.7, 22.9\,\mu$m; width $w = 8.0, 8.4, 16.6\,\mu$m respectively for CR, TS, OM), but differ strongly in swimming mechanism. The two algal species are pulled by apical flagella, two for CR and four for TS, beating with similar waveforms but species-specific gaits: an oscillating synchronous breaststroke for CR [52]; a smooth transverse gallop for TS [53]. Both are, on average, puller-type microswimmers [4, 54, 55]. The dinoflagellate OM possesses two flagella at the back of its body: a short lateral one used to turn and to aid in feeding [56]; and a longer one pushing the cell forward. It is therefore a pusher-type microorganism [56]. The three organisms swim with characteristic velocities $v_S = 49, 116, 119\ \mu$m.s^{-1}(CR, TS, OM).

Numerical simulations

Inspired by previous work [30, 46, 57–59] we develop a self-propelled swimmer model, named the 'outboard swimmer'. This name implies that all propulsion forces are transmitted to the liquid from outside the cell body, as opposed to be generated at the swimmer surface. For example, the helical flagellum of a bacterium bears resemblance to an outboard motor, while CR takes after a rowing boat. To capture the near-field flows of an organism, we use a finite-sized spherical body (radius r_S) with a *no-slip* boundary condition at its surface. Propulsion is achieved by a set of regularised Stokeslets outside the body, whose flow satisfies the no-slip condition on the cell body. The number, arrangement and motion of the driv-

ing forces is species specific. Instantaneous swimming speed and rotation derive from the requirement of zero net force and torque. SI §3-6 contain a complete presentation of the model and the resulting swimmer-generated flow fields $\boldsymbol{u}(\boldsymbol{x},t)$. This model will be used to simulate an actively beating CR, a steady OM, and a steady *E. coli* (EC) bacterium for comparison. The swimmers' size and stroke-averaged speed are $r_{\mathrm{S}} = 3.5, 9, 0.5$ μm and $v_{\mathrm{S}} = 84, 100, 25$ μm.s^{-1} (CR, OM, EC). Tracer particles of radius r_{P} are advected by the swimmer-generated velocity field according to Faxén's laws, $\boldsymbol{v} = (1 + \frac{1}{6} r_{\mathrm{P}}^2 \nabla^2)\boldsymbol{u}$, interact with the swimmer through hard-core repulsion, and diffuse with bulk diffusivity D according to the Stokes-Einstein equation.

RESULTS

Nearby object-microswimmer interactions are governed by a universal entrainment mechanism

When inspecting tracer dynamics at large magnification (×100) and high framerate (500 fps), very similar entrainment events are observed for all our organisms, regardless of their propulsion mechanism or generated flow. Examples of typical trajectories with particle radius $r_{\mathrm{P}} = 0.5$ μm are shown in Videos S1-3, for CR, TS and OM respectively. This mechanism is best understood from the viewpoint co-moving with the swimmer. After an almost head-on collision, a bead reaches a region near the cell surface, Fig. 1a. It travels slowly around the body approximately following streamlines from front to back, and eventually leaves behind the organism, Fig. 1b-c. Since the only common physical feature of these organisms is the presence of the cell body surface, we propose that entrainment is only the consequence of the *no-slip* layer that this boundary induces. Therefore, the particle is hydrodynamically coupled to the swimmer in this layer and resides in its vicinity for an extended duration, the contact time T. In the laboratory frame, the particle is then displaced a distance L in the direction of motion. Hence, the average contact time and entrainment length are directly related via

$$\langle L \rangle \approx v_{\mathrm{S}} \langle T \rangle. \tag{1}$$

To quantify our observations, we measure the distribution of L for different swimmers, Fig. 1e. These all have the same shape, indicating that the mechanism is comparable, with an exponential decay of length scale $L_{\mathrm{J}}^{(\mathrm{S})}$ above the length $L_{\mathrm{M}}^{(\mathrm{S})}$ at the peak of the distribution. Exponential fits to these curves give $L_{\mathrm{J}}^{(\mathrm{CR})} = 9.2 \pm 0.6$ μm for CR, $L_{\mathrm{J}}^{(\mathrm{TS})} = 7.4 \pm 1.2$ μm for TS and $L_{\mathrm{J}}^{(\mathrm{OM})} = 11.7 \pm 1.4$ μm for OM, while we find $L_{\mathrm{M}}^{(\mathrm{CR})} \approx 6.7$ μm, $L_{\mathrm{M}}^{(\mathrm{TS})} \approx 8.6$ μm and $L_{\mathrm{M}}^{(\mathrm{OM})} \approx 7.5$ μm.

Surprisingly, the characteristic entrainment length $L_{\mathrm{J}}^{(\mathrm{S})}$ is significantly smaller for TS than CR despite a slightly larger body size. As described also in SI §2, this effect is mainly attributed to the larger number of flagella in TS, which limit the average contact time by either rapidly pushing the beads backwards during the power stroke (Video S2) or by ejecting them out of the no-slip layer during the recovery stroke. However, at the same time, front-mounted flagella can reach out and pull beads towards the body, widening the effective cross-section for entrainment around the swimming path. This is reflected in PDF($\tilde{b}$ | jump), the distribution of rescaled impact parameters, $\tilde{b} = 2b/w$, before entrainment. For both TS and OM, PDF($\tilde{b}$ | jump) can be described accurately by a single exponential decay with characteristic lengths $\tilde{b}^{(\mathrm{TS})} = 1.0 \pm 0.3$ and $\tilde{b}^{(\mathrm{OM})} = 0.70 \pm 0.25$ (Fig. 1g,h). However, with CR, structurally very similar to TS but with a single pair of flagella, the distribution shows two markedly distinct behaviours for impact parameters above and below the cell body radius. For $\tilde{b} > 1$, PDF($\tilde{b}$ | jump) follows the curve characteristic of TS; below that threshold we observe instead an exponential decay with a significantly smaller characteristic length $\tilde{b}^{(\mathrm{CR})} = 0.30 \pm 0.05$. This is a consequence of the fact that, in CR, entrainments below $\tilde{b} \sim 1$ are overwhelmingly the consequence of "pure" collisions with the cell body, without appreciable influence from flagella. Flagella participate instead in entrainment events with relatively large impact parameters, by increasing significantly their abundance over what would otherwise be expected. In order to study the main entrainment mechanism for CR, in the following we will focus on jump events with $\tilde{b} < 0.75$ when comparing with numerical data. These include $\sim 70\%$ of all the entrainments observed.

The outboard swimmer model captures the entrainment mechanism faithfully. Figures 1c,d show that simulated tracer trajectories reproduce well the experimental ones. In particular, we see that in both cases the particles tend to detach close to the swimming axis despite the variation in initial impact parameter, here randomly chosen in $[0, r_{\mathrm{S}}]$ (see also Videos S4,5 for CR and OM resp. and Video S6 for a comparison with EC). More quantitatively, the PDF of entrainment lengths from simulations compares very well with the experimental one, Fig. 1f, although the entrainment length is globally overestimated ($L_{\mathrm{M}}^{(\mathrm{sim})} \approx 14.5$ μm and $L_{\mathrm{M}}^{(\mathrm{exp})} \approx 9.4$ μm). We attribute this discrepancy to approximations within this minimal model, chiefly the assumption of straight swimming, and possibly further interactions with flagella.

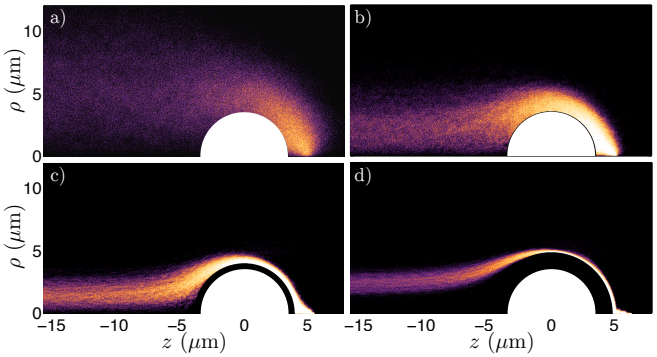

FIG. 2. Entrainment simulations by the outboard swimmer of Brownian tracer particles of various sizes. Shown are spatial PDFs of the beads, azimuthally and time-averaged, as seen in the co-moving frame of a CR alga, obtained by averaging over an ensemble of 10^3 particles released in front of the body at $b = 0$ μm with a constant surface-to-surface distance of 1.5 μm. a) Small tracers with $r_{\mathrm{P}} = 0.01$ μm diffuse away quickly and are not entrained for a long time. b-c) Intermediate-sized tracers with $r_{\mathrm{P}} = 0.072, 0.52$ μm primarily flow along streamlines close to the swimmer body, in its no-slip layer, and are the furthest entrained. d) Large tracers with $r_{\mathrm{P}} = 1.38$ μm flow along paths far from the swimmer body, and are entrained less.

Steric interactions reduce the contact time of large particles

In light of these findings about the entrainment mechanism, we will now develop a simple theory to predict contact times. A detailed derivation is given in SI §7. We consider small particles that do not disturb the swimming direction significantly, which is a reasonable assumption if $r_{\mathrm{P}} \lesssim r_{\mathrm{S}}$ [47] as supported also by our experiments. A streamline along the swimmer body can be approximated as

$$r_{\mathrm{SL}}(\theta, b) \approx r_{\mathrm{S}} + b\sqrt{2/3}/\sin\theta, \tag{2}$$

written in spherical coordinates of the reference frame co-moving with the swimmer, Fig. 1b. Close to the cell body the advection of tracers is then governed by the tangential flow, $u_\theta(r, \theta)$. Evaluating u_θ along a streamline with impact parameter b gives the velocity of a particle,

$$u_\theta[r_{\mathrm{SL}}(b)] = \frac{3v_{\mathrm{S}}\epsilon_0}{2r_{\mathrm{S}}}\frac{1}{g(\lambda)} + \mathcal{O}\left(\epsilon_0^2\right), \tag{3}$$

$$g(\lambda) = \left(1 + \frac{3\lambda^3(1+\lambda)^2}{(1+2\lambda)(1+\lambda^2)^{5/2}}\right)^{-1}, \tag{4}$$

where $\epsilon_0 = r_{\mathrm{SL}}(\pi/2) - r_{\mathrm{S}} = b\sqrt{2/3}$ is the closest distance of approach, Fig. 1b, and $g(\lambda) \in [0, 1]$ characterises the flagellar distance from the body ($\lambda = 2, 4, 5$ for OM, CR and EC respectively, see SI §7A-B). Then, in the deterministic limit, the contact time is found by integrating the inverse velocity along the particle trajectory, $T \approx \int ds/v_\theta$, where ds is the arclength differential. Since the velocity satisfies the no-slip condition at the cell surface, tracers with a small distance of approach ϵ_0 move around the body slowly (Eq. 37) which increases the contact time. As the minimum distance is dictated by the finite size of the particle, larger tracers are expected to experience stronger tangential flows and therefore smaller contact times.

Brownian noise limits entrainment of small particles

Together with particle advection, it is important to consider the presence of thermal noise. We first explore its effect by simulating outboard swimmers with tracers subjected to Brownian motion (Videos S4-6). Figure 2 shows how the spatial PDF of an ensemble of tracers initially in front of the microorganism depends on tracer size. Small tracers spread far from the swimmer and do not efficiently access the no-slip layer (Fig. 2a). Consequently, they are exposed to stronger tangential flows, limiting the contact time. Large tracers do not diffuse away but cannot approach the no-slip surface closely, as described previously and illustrated by the inaccessible region around the cell body (Fig. 2d). Instead, we see a maximum in the contact time for beads of intermediate size, which concentrate most tightly around the moving cell (Fig. 2b,c). Optimal entrainment is systematically observed in simulations of both OM and CR, with optimal tracer radii $r_{\mathrm{P}}^* \sim 0.4, 0.3$ μm respectively (Fig. 3a). Moreover, whereas these organisms can move particles along for ~ 5 body lengths, entrainments by the EC model do not exceed ~ 1.2 μm for any tracer size. The super-linear growth of the average jump length on cell size (Fig. S8c and [46]) strongly restricts particle transport for micron-size organisms, and is consistent with the lack of previous reports of strong entrainment by bacteria [60–63].

Experiments with CR for a range of different tracer sizes confirm the existence of a maximum in entrainment length (Fig. 3b), with diffusion-dominated tracer trajectories below, and steric-interaction-limited paths above, the optimal size $r_{\mathrm{P}}^* \sim 0.7$ μm. These features are observed in simulations also when considering tracers that are initially located at random impact parameters b within $[0, r_{\mathrm{S}}]$, rather than directly in front of the cell (Fig. 3b inset). Altogether, the semi-quantitative agreement on both the location of the maximum and the values of jump lengths suggests that our outboard model captures the essential physics behind the entrainment mechanism.

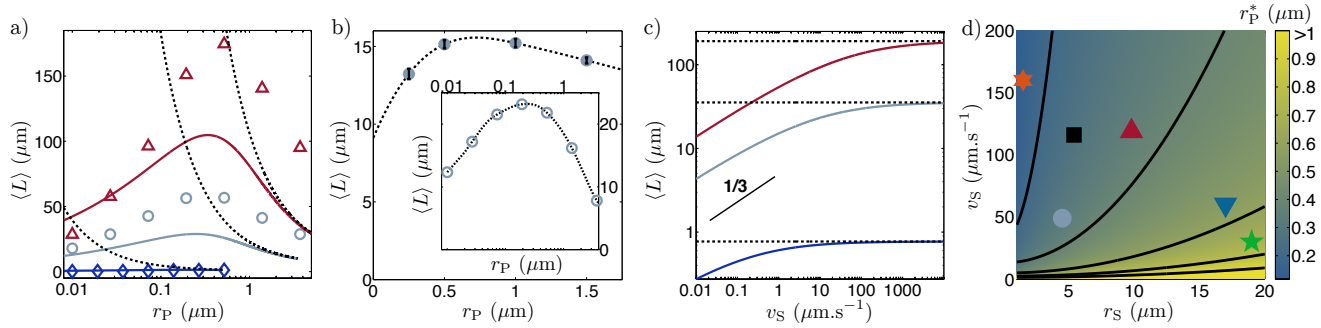

FIG. 3. Average entrainment length $\langle L\rangle$ as a function of tracer size: a) Simulated as in Fig. 2 for OM, CR, and EC (open red triangles, grey circles and blue diamonds respectively). The initial surface-to-surface distance is 11 μm for OM, 1.5 μm for CR, and 0.5 μm for EC. Solid lines show the corresponding analytical prediction; dashed lines without noise. Same data on log-log scale in Fig. S8b. b) Average entrainment length obtained experimentally with CR for different tracer sizes. Inset: Same data obtained in simulations with tracers initially located in front of the swimmer at impact parameters b uniformly distributed in $[0, r_S]$. Dashed lines are guides to the eye. c) Analytical $\langle L\rangle$ as a function of swimming speed at fixed $r_P = 1$ μm (Solid lines; OM red, CR grey, EC blue. Dashed lines; without noise). d) The optimal bead size r_P^* as a function of swimmer size and speed, obtained from equation 49 with constant value $\lambda = 4$. Markers represent a few typical model organisms; grey circle: CR, black square: TS, red pyramid: OM, blue triangle: *Euglena gracilis*, green star: *Peranema trichophorum*, six-pointed orange star: *Bdellovibrio bacteriovorus*.

Optimum in contact time with tracer size

We rationalise these findings using a theory akin to Taylor's dispersion [64, 65]. Consider a Brownian particle advected in a linear shear flow over a straight solid surface that mimicks the swimmer's cell wall, Fig. 4a. The flow velocity is $\boldsymbol{u} = \epsilon U \boldsymbol{e}_x$, where the strain rate, $U = 3v_S/(2r_S g(\lambda))$, derives from the velocity along a streamline given by Eq. 37. A particle of radius r_P is initially positioned at $(x = 0, \epsilon = r_P)$, disperses with diffusivity D and is advected by the flow $\boldsymbol{u}(\epsilon)$, but cannot cross the line $\epsilon = r_P$. Without loss of generality, this is mapped to an unbounded "image" system [66] where the particle is initially located at $(x = 0, y = 0)$, the modified flow is $\boldsymbol{v} = (r_P + |y|)U\boldsymbol{e}_x$, and the tracer can diffuse everywhere (Fig. 4b).

With this model we aim to compute the average time $\langle T\rangle$ needed for the colloid to travel a distance $\pi(r_S + r_P)$ along the positive x-direction, imitating a journey around the swimmer body. The corresponding stochastic equations of motion are

$$\dot{x}(t) = \big(r_P + |y|\big)U + \xi_x(t), \quad \dot{y}(t) = \xi_y(t), \tag{5}$$

with an uncorrelated Gaussian noise, $\boldsymbol{\xi}$, that satisfies $\langle \xi_i\rangle = 0$ and $\langle \xi_i(t)\xi_j(t')\rangle = 2D\delta_{ij}\delta(t-t')$. Integrating and ensemble averaging Eq. 43 (see SI § 7D), leads to

$$\langle x(t)\rangle = r_P U t + \frac{4\sqrt{D}}{3\sqrt{\pi}} U t^{3/2}. \tag{6}$$

The mean time $\langle T\rangle$ is then the solution of the cubic equation

$$0 = c_0 + c_2\langle T\rangle + c_3\langle T\rangle^{3/2}, \tag{7}$$

$$c_0 = -\frac{2\pi r_S(r_S + r_P)g(\lambda)}{3v_S r_P};\ c_2 = 1;\ c_3 = \frac{4\sqrt{D}}{3r_P\sqrt{\pi}}, \tag{8}$$

which is solved analytically using the Cardano formula. The average entrainment length $\langle L\rangle$, obtained from Eq. 1, is shown with solid lines in Fig. 3a for CR, OM and EC, using the same parameters as in the simulations. We see good agreement for the position of the maximum and the overall shape of the curve. The predicted magnitude of the entrainment length deviates by a factor of ~ 2 near the maxima, due mostly to an overestimate of the average tangential speed experienced by the tracer (see Fig. S8a and SI §7E).

We recover the deterministic limit as $D \to 0$ (see [46] and SI §7C), Fig. 3a dashed lines. In this limit, the entrainment length does not depend on the swimming speed (Fig. 3c dashed lines). However, when taking thermal noise into account, $\langle L\rangle \sim v_S^{1/3}$ as $v_S \to 0$ (Fig. 3c solid lines): The slower the organism, the shorter the entrainment length because particles diffuse away before being displaced substantially. Altogether, our results show that Brownian motion can have a significant effect on the entrainment efficiency.

Factors controlling the optimal particle size and predation

The optimal tracer size r_P^* can be tuned by varying the swimmer size and speed. Fig. 3d presents a map of r_P^*, obtained by optimising the contact time (Eq. 49)

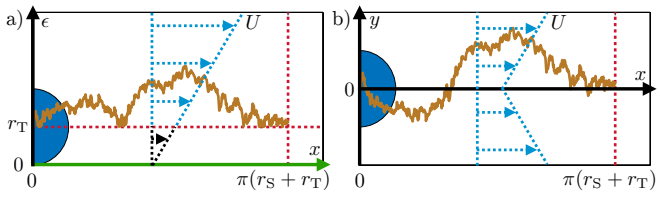

FIG. 4. Schematics of the analytical model: a) A Brownian particle is advected over a solid surface (green axis) in a linear shear flow along the x-direction characterized by a strain rate U. The tracer of radius r_P, initially located at $x = 0$ and $\epsilon = r_P$, is free to diffuse in any direction but cannot cross the line $\epsilon = r_P$ due to steric interactions. b) In the equivalent image system, the tracer is free to diffuse through the surface $y = 0$, but with a modified flow that is non-zero at the wall and always positive.

with varying r_S and v_S but fixed $\lambda = 4$. On one hand, increasing swimmer speed v_S shifts r_P^* to lower values, because faster advection limits the importance of Brownian motion. On the other, increasing swimmer size r_S increases r_P^*, because the larger distance to travel around the cell enhances the relative effect of diffusion. A simple estimate for the optimal particle size is found by comparing a characteristic diffusion time $\tau_{diff} \sim r_P^2/(2D)$ and a characteristic advection time $\tau_{adv} \sim 2\pi r_S^2/(3v_S r_P)$ from Eq. 37. Defining the entrainment Péclet number as $Pe = 3v_S r_P^4/(4\pi \tilde{D} r_S^2)$, $\tilde{D} = r_P D$, the optimal tracer size corresponds to $Pe = 1$:

$$r_P^* \approx \sqrt[4]{4\pi r_S^2 \tilde{D}/3v_S}. \tag{9}$$

This expression gives reasonable quantitative estimates, $r_P^* \sim 0.8$ μm for CR, using the parameters from our experiments. The power law dependences of r_P^* on r_S and v_S are also consistent with numerical solutions of Eq. 49 (Fig. S9).

Whereas we have solely discussed motile cells with passive objects until now, it is worthwhile considering situations where both parties are active, as found in many predator-prey systems. Prey motility could affect the contact time substantially, notably because it could help turn and escape. Prey velocity v_P and its reorientation timescale τ_r, lead to effective diffusion coefficients $D_{eff} = v_P^2 \tau_r$, which can be ~ 100 times larger than D for typical bacteria [67, 68]. This gives another Péclet number, $Pe = 3v_S r_P^3/(4\pi \tau_r v_P^2 r_S^2)$, which can be significantly smaller than the previous one, signaling a possibly substantial decrease in contact time. Therefore, even though prey motility increases encounter rates with predators [69], it could nonetheless reduce the overall probability of being captured.

DISCUSSION

Swimming microorganisms vary greatly both in body size and in the details of their propulsion, from the number and arrangement of flagella to their gaits. Yet, despite this variability, our results show that particle entrainment is a remarkably universal mechanism. Combining experiments with numerical simulations, we see that pullers and pushers entrain particles with similar efficiency. We see no evidence for either "wake bubble" effects [49], or entrainment due to a stagnation point in front of the cell [48, 50]. Instead, our results suggest that entrainment is a consequence of an organism's *no-slip* surface, a characteristic shared by the three species we study here. This feature, recently suggested also in [46], is consistent with the lack of entrainment in numerical studies involving squirmers, which instead propel with a surface slip velocity [49, 50]. Accordingly, we predict that ciliates like *Paramecium* and multicellular algae like *Volvox* will not substantially entrain micron-sized objects, since they swim by an effective surface slip generated by thousands of cilia and flagella. Studies of *V. carteri* swimming through a colloidal suspension support this hypothesis (see supplementary movie from [3]). Comparing different species, we also see that the flagellar arrangement has a quantitative effect on particle entrainment. Front-mounted flagella decrease the average contact time T but increase the interaction range, and are therefore likely to increase the frequency of entrainments.

The outboard model proves to be in fair qualitative and quantitative agreement with our experimental results. It provides directly comparable tracer dynamics and, crucially, it successfully reproduces the shape of the entrainment length distribution. This strongly suggests that the model correctly captures the essential physics, with further support provided by the maximum in the entrainment length over particle size observed in both experiments and simulations. The particle size for optimal entrainment and longest contact, r_P^*, is set by a combination of thermal noise and steric interactions. This can be captured accurately by a Taylor-dispersion theory which, in turn, provides a general prediction for the contact time T and its dependence on organism size and speed.

Size-dependent contact times might affect predation by microorganisms. Experimental studies of microbial grazing indicate that this is indeed a selective process [70]. For example, *Oxyrrhis marina* feeds on prey ranging from bacteria to cells as large as itself [35, 71], but seems to have an optimal prey size [35, 36, 72, 73], in agreement with our hydrodynamic arguments. Phagotrophic selectivity is complex, and certainly depends on many factors including chemical cues and cell surface properties. However, the physics leading to the non-monotonic size-dependence of contact time is inescapable, and therefore needs to be taken into account. A non-monotonic de-

pendence on tracer size has also been reported for the effective diffusion of colloidal particles suspended within an *E. coli* culture [74]. These experiments, which focus on particles larger than the microorganisms, show that potentially new mechanisms could be at play in that size range.

To conclude, we have seen that particle entrainment is a generic feature of the interaction between microorganisms and small particles, and have characterised the physics behind it. A complete picture of these interactions, however, will require to integrate our results not only with those from intermediate and far-field studies [45, 75], but also with a thorough characterisation of the navigational strategy of the microorganism [76]. This will enable more accurate bottom-up models of microbial grazing, which can be used to predict feeding or clearance rates by phagotrophs [30], and potential tradeoffs between feeding and swimming [25, 37, 77]. At the same time, prolonged contact also underpins the successful binding of viruses and other parasites to cells [32]. By showing that the contact time with motile microorganisms is limited, $\lesssim 3$ s for reasonable swimmer sizes and speeds, we suggest that motility can potentially affect infection rates [33] and thus provide a fitness advantage. This should be true in particular for ciliates, which display an effective surface slip and therefore a faster clearance of particles. Targeted experiments and modelling efforts in this area will improve our mechanistic understanding of early infection events in microorganisms.

From a micro-engineering perspective, our model shows that entrainment lengths become millimetric or even larger for micrometric tracers when considering swimmers or active particles with radius $r_s \gtrsim 50\ \mu$m. When combined with externally triggered reorientation events, this purely hydrodynamic phenomenon could enable cargo transport by self-propelled colloids without requiring any surface functionalisation.

Acknowledgements:
We are grateful to Kirsty Wan and Raymond Goldstein for sharing the initial culture of TS. This work was supported in part by and ERC Advanced Grant (291234 MiCE) (A.M.); and a Royal Society Research Grant (RG150421) (M.P.).

* A.M. and R.J. contributed equally to this work and are joint lead authors.
† A.M., R.J. and M.P. designed the study, analysed results and wrote the manuscript; R.J. performed the experiments; A.M. developed the model, performed simulations, and formed the theory.
‡ Correspondence: M.Polin@warwick.ac.uk

[1] A. Prindle, J. Liu, M. Asally, S. Ly, J. Garcia-Ojalvo, G. M. Suel, and G. M. Süel, Nature **527**, 59 (2015), arXiv:15334406.
[2] J. N. Wilking, V. Zaburdaev, M. De Volder, R. Losick, M. P. Brenner, and D. a. Weitz, Proc. Natl. Acad. Sci. U. S. A. **110**, 848 (2013).
[3] K. Drescher, R. E. Goldstein, N. Michel, M. Polin, and I. Tuval, Phys. Rev. Lett. **105**, 168101 (2010).
[4] J. S. Guasto, K. a. Johnson, and J. P. Gollub, Phys. Rev. Lett. **105**, 168102 (2010), arXiv:1008.2535.
[5] K. Drescher, J. Dunkel, L. H. Cisneros, S. Ganguly, and R. E. Goldstein, Proc. Natl. Acad. Sci. U. S. A. **108**, 10940 (2011).
[6] H. P. Zhang, A. Be'er, E.-L. Florin, and H. L. Swinney, Proc. Natl. Acad. Sci. U. S. A. **107**, 13626 (2010).
[7] L. H. Cisneros, R. Cortez, C. Dombrowski, R. E. Goldstein, and J. O. Kessler, Anim. Locomot. , 99 (2010).
[8] A. Sokolov and I. S. Aranson, Phys. Rev. Lett. **109**, 248109 (2012) (2012).
[9] S. Lai, J. Tremblay, and E. Déziel, Environ. Microbiol. **11**, 126 (2009).
[10] M. T. Butler, Q. Wang, and R. M. Harshey, Proc. Natl. Acad. Sci. U. S. A. **107**, 3776 (2010).
[11] A. Sokolov and I. S. Aranson, Phys. Rev. Lett. **103**, 148101 (2009).
[12] S. Rafaï, L. Jibuti, and P. Peyla, Phys. Rev. Lett. **104**, 098102 (2010), arXiv:0909.4193.
[13] H. M. López, J. Gachelin, C. Douarche, H. Auradou, and E. Clément, Phys. Rev. Lett. **115**, 028301 (2015), 1503.0551.
[14] H. Wioland, F. G. Woodhouse, J. Dunkel, J. O. Kessler, and R. E. Goldstein, Phys. Rev. Lett. **110**, 268102 (2013), arXiv:1304.2875.
[15] A. J. T. M. Mathijssen, A. Doostmohammadi, J. M. Yeomans, and T. N. Shendruk, J. R. Soc. Interface **13**, 20150936 (2016).
[16] M. Ravnik and J. M. Yeomans, Phys. Rev. Lett. **110**, 026001 (2013).
[17] E. Lushi, H. Wioland, and R. E. Goldstein, Proc. Natl. Acad. Sci. U. S. A. **111**, 9733 (2014).
[18] A. J. T. M. Mathijssen, A. Doostmohammadi, J. M. Yeomans, and T. N. Shendruk, J. Fluid Mech. **806**, 35 (2015).
[19] J. R. Platt, Science **133**, 1766 (1961).
[20] M. S. Plesset and H. Winet, Nature **248**, 441 (1974).
[21] T. J. Pedley, N. a. Hill, and J. O. Kessler, J. Fluid Mech. **195**, 223 (1988).
[22] I. Tuval, L. Cisneros, C. Dombrowski, C. W. Wolgemuth, J. O. Kessler, and R. E. Goldstein, Proc. Natl. Acad. Sci. U. S. A. **102**, 2277 (2005).
[23] J. Dervaux, M. Capellazzi Resta, and P. Brunet, Nat. Phys. **13**, 306 (2016).
[24] V. Magar, T. Goto, and T. J. Pedley, Q. J. Mech. Appl. Math. **56**, 65 (2003).
[25] S. Michelin and E. Lauga, Phys. Fluids **23**, 101901 (2011), arXiv:1109.0112.
[26] D. Tam and a. E. Hosoi, Proc. Natl. Acad. Sci. U. S. A. **108**, 1001 (2011).
[27] A. Doostmohammadi, R. Stocker, and A. Ardekani, Proc. Nat. Ac. Sci. U. S. A. **109**, 3856 (2012).
[28] R. A. Lambert, F. Picano, W.-P. Breugem, and L. Brandt, J. Fluid Mech. **733**, 528 (2013).
[29] T. Ishikawa, S. Kajiki, Y. Imai, and T. Omori, J. Fluid Mech. **789**, 481 (2016).
[30] J. Dölger, L. T. Nielsen, T. Kiørboe, and A. Andersen, Sci. Rep. **7**, 39892 (2017).
[31] M. B. Short, C. a. Solari, S. Ganguly, T. R. Powers, J. O.

Kessler, and R. E. Goldstein, Proc. Natl. Acad. Sci. U. S. A. **103**, 8315 (2006).
[32] G. Seisenberger, M. U. Ried, T. Endress, H. Büning, M. Hallek, and C. Bräuchle, Science **294**, 1929 (2001).
[33] T. B. Taylor and A. Buckling, J. Evol. Biol. **26**, 2154 (2013).
[34] J. A. Riffell and R. K. Zimmer, J. Exp. Biol. **210**, 3644 (2007).
[35] E. C. Roberts, E. C. Wootton, K. Davidson, H. J. Jeong, C. D. Lowe, and D. J. Montagnes, J. Plankt. Res. **33**, 603 (2010).
[36] K. Davidson, F. Sayegh, and D. J. Montagnes, J. Plankt. Res. **33**, 651 (2011).
[37] W. Gilpin, V. N. Prakash, and M. Prakash, Nat. Phys. **AOP** (2016), 10.1038/nphys3981, arXiv:1611.01173.
[38] M. Cole, P. Lindeque, E. Fileman, C. Halsband, R. Goodhead, J. Moger, and T. S. Galloway, Environ. Sci. Tech. **47**, 6646 (2013).
[39] S. L. Wright, R. C. Thompson, and T. S. Galloway, Environ. Pollution **178**, 483 (2013).
[40] M. Bally, A. Gunnarsson, L. Svensson, G. Larson, V. P. Zhdanov, and F. Höök, Phys. Rev. Lett. **107**, 188103 (2011).
[41] A. Banerjee, A. Berezhkovskii, and R. Nossal, Phys. Biol. **13**, 016005 (2016), arXiv:1411.7348.
[42] H. Xu and D. E. Shaw, Biophys. J. **110**, 218 (2016).
[43] E. M. Purcell, Am. J. Phys **45**, 3 (1977).
[44] C. Darwin, Math. Proc. Cambridge Philos. Soc. **49**, 342 (1953).
[45] D. O. Pushkin, H. Shum, and J. M. Yeomans, J. Fluid Mech. **726**, 5 (2013).
[46] P. Mueller and J.-L. Thiffeault, Phys. Rev. Fluids **2**, 013103 (2017).
[47] H. Shum and J. M. Yeomans, In Press (2017).
[48] R. Jeanneret, D. O. Pushkin, V. Kantsler, and M. Polin, Nat. Commun. **7**, 12518 (2016), arXiv:1602.01666.
[49] Z. Lin, J.-L. Thiffeault, and S. Childress, J. Fluid Mech. **669**, 167 (2011), arXiv:1007.1740.
[50] J.-L. Thiffeault, Phys. Rev. E **92**, 023023 (2015).
[51] J. Rochaix, S. Mayfield, M. Goldschmidt-Clermont, and J. Erickson, Plant molecular biology: a practical approach. IRL Press, Oxford , 253 (1988).
[52] M. Polin, I. Tuval, K. Drescher, J. P. Gollub, and R. E. Goldstein, Science **325**, 487 (2009).
[53] K. Y. Wan and R. E. Goldstein, Proc. Natl. Acad. Sci. U. S. A. **113**, E2784 (2016), arXiv:1510.03272.
[54] E. Lauga and T. R. Powers, Reports Prog. Phys. **72**, 096601 (2009).
[55] G. S. Klindt and B. M. Friedrich, Phys. Rev. E **92**, 063019 (2015), arXiv:1504.05775v1.
[56] T. Kiørboe, H. Jiang, R. J. Goncalves, L. T. Nielsen, and N. Wadhwa, Proc. Natl. Acad. Sci. U. S. A. **111**, 11738 (2014).
[57] R. R. Bennett and R. Golestanian, Phys. Rev. Lett. **110**, 148102 (2013).
[58] B. M. Friedrich and F. Jülicher, Phys. Rev. Lett. **109**, 138102 (2012).
[59] D. R. Brumley, K. Y. Wan, M. Polin, and R. E. Goldstein, eLife **3**, e02750 (2014).
[60] X.-L. Wu and A. Libchaber, Phys. Rev. Lett. **84**, 3017 (2000).
[61] T. Ishikawa, J. T. Locsei, and T. J. Pedley, Phys. Rev. E **82**, 021408 (2010).
[62] T. V. Kasyap, D. L. Koch, and M. Wu, Phys. Fluids **26**, 081901 (2014).
[63] A. Jepson, V. A. Martinez, J. Schwarz-Linek, A. Morozov, and W. C. K. Poon, Phys. Rev. E **88**, 041002(R) (2013), arXiv:1307.1274.
[64] G. Taylor, Proc. Roy. Soc. Lond. A **219**, 186 (1953).
[65] H. A. Stone, A. D. Stroock, and A. Ajdari, Ann. Rev. Fluid Mech. **36**, 381 (2004).
[66] N. G. Van Kampen, *Stochastic processes in physics and chemistry* (Elsevier, Amsterdam, 1983).
[67] H. C. Berg, *Random walks in biology* (Princeton University Press, 1993).
[68] J. Saragosti, P. Silberzan, and A. Buguin, PloS one **7**, e35412 (2012).
[69] R. Almeda, H. van Someren Gréve, and T. Kiørboe, Ecosphere **8** (2016), 10.1002/ecs2.1668.
[70] D. J. S. Montagnes, A. B. Barbosa, J. Boenigk, K. Davidson, K. Jürgens, M. Macek, J. D. Parry, E. C. Roberts, and K. Šimek, Aquat. Microb. Ecol. **53**, 83 (2008).
[71] K. J. Flynn, K. Davidson, and A. Cunningham, J. Exp. Mar. Biol. Ecol. **196**, 357 (1996).
[72] P. J. Hansen, Marine Biology **114**, 327 (1992).
[73] F. C. Hansen, H. J. Witte, and J. Passarge, Aquat. Microb. Ecol. **10**, 307 (1996).
[74] A. E. Patteson, A. Gopinath, P. K. Purohit, and P. E. Arratia, Soft matter **12**, 2365 (2016).
[75] A. J. T. M. Mathijssen, D. O. Pushkin, and J. M. Yeomans, J. Fluid Mech. **773**, 498 (2015).
[76] V. Méndez, D. Campos, and F. Bartumeus, *Stochastic Foundations in Movement Ecology: Anomalous Diffusion, Front Propagation and Random Searches*, Springer Series in Synergetics (Springer Berlin Heidelberg, 2013).
[77] R. R. Strathmann and D. Grünbaum, Integr. Compar. Biol. **46**, 312 (2006).
[78] S. E. Spagnolie, G. R. Moreno-Flores, D. Bartolo, and E. Lauga, Soft Matter **11**, 3396 (2015).
[79] S. Kim and S. J. Karilla, *Microhydrodynamics* (Dover, New York, 1991).

SUPPLEMENTARY INFORMATION: UNIVERSAL ENTRAINMENT MECHANISM CONTROLS CONTACT TIMES WITH MOTILE CELLS

CONTENTS

Introduction 1

Materials and Methods 2

Results 3

Discussion 6

References 7

Supplementary Information: Universal entrainment mechanism controls contact times with motile cells 9

Experimental methods 9

On the effect of flagella 10

Model for *Chlamydomonas* 11

Model for *E. coli* 13

Model for *Oxyrrhis marina* 14

Simulating the outboard model 15

Contact time theory 15

EXPERIMENTAL METHODS

Introduction to the microorganisms

We have considered 3 different species of eukaryotic microorganisms presenting different features of swimming but having roughly the same body-size: Chlamydomonas reinhardtii (CR), Tetraselmis subcordiforms (TS) and Oxyrrhis marina (OM). CR and TS are both unicellular algae having very similar prolate body shape but differing by the number of flagella in front of their body: 2 for CR and 4 for TS. CR uses most of the time a breaststroke way of swimming, while TS flagella beat successively in a transverse gallop fashion [53]. The length and width of their body are respectively $\langle l^{(\mathrm{CR})}\rangle = 10.1 \pm 1.7\mu$m and $\langle w^{(\mathrm{CR})}\rangle = 8.0 \pm 1.7\mu$m for CR, $\langle l^{(\mathrm{TS})}\rangle = 13.7 \pm 1.9\mu$m and $\langle w^{(\mathrm{TS})}\rangle = 8.4 \pm 1.0\mu$m for TS. In the (confined) microfluidic channels (thickness $h = 25.8 \pm 0.1\mu$m) used for the experiments, the average speed of these microorganisms were: $\langle v^{(\mathrm{CR})}\rangle = 49.1 \pm 2.5\mu\mathrm{m.s}^{-1}$ and $\langle v^{(\mathrm{TS})}\rangle = 116 \pm 6\mu\mathrm{m.s}^{-1}$. OM is a dinoflagellate found pretty much in all oceans around the world (except the polar seas). During the past twenty years this microorganism has become a model organism for studying predator-prey interactions at the micro-scale. It also has a prolate shape but is bigger and more asymmetric than CR and TS. We measured an average length $\langle l^{(\mathrm{OM})}\rangle = 22.9 \pm 3.4\mu$m, an average width $\langle w^{(\mathrm{OM})}\rangle = 16.6 \pm 1.8\mu$m and an average speed (in a 29μm-thick channel) $\langle v^{(\mathrm{OM})}\rangle = 119 \pm 10\mu\mathrm{m.s}^{-1}$. This microorganism has 2 flagella at the back of its body a long and a short one. The long one is used to propel while the short transverse one is used to turn and appears to be a tool to catch and recognize preys. We chose this microorganism as a representative of eukaryotic pusher-type swimmers.

Cultures of the microrganisms

Cultures of *Chlamydomonas reinhardtii* (CR) strain CC125 were grown axenically in a Tris-Acetate-Phosphate medium at 21° C under periodic fluorescent illumination ($100\,\mu\mathrm{E/m^2s}$, OSRAM Fluora) with a dark/light cycle of 12h/12h. This is done to synchronize the cell cycles among the population. Given their large growth factor ($\sim 4-6$ cells/day), cultures were kept at a concentration of $\sim 5.10^6$ cells/ml in the exponential phase by transfering daily the algae into a new flask of fresh-medium.

Cultures of *Tetraselmis subcordiforms* (TS) strain CCAP 161/1A were grown axenically in a Seawater Nutrient Broth medium at 21° C under fluorescent illumination ($100\,\mu\mathrm{E/m^2s}$, OSRAM Fluora). Cultures were kept at a concentration of $\sim 10^6$ cells/ml by transfering biweekly the algae into a new flask of fresh-medium (growth factor ~ 1.4 cells/day).

Cultures of *Oxyrrhis marina* (OM) strain CCAP 1133/5 were grown monoxenically in a f/2 medium at 21° C together with the small alga *Nannochloropsis oculata* (CCAP 849/1) serving as food. Fresh medium and algae were supplied to the culture every $\sim 1-2$ months.

Experimental setup

After gently centrifuging the suspension of a given organism, the supernatant was replaced by the appropriate fresh medium also containing a small fraction of colloids. The suspension was then loaded into a PDMS based microfluidic chip having a visualisation chamber 2 mm wide and $\sim 26\mu$m (for CR and TS) or $\sim 29\mu$m thick (for OM). The channels were previously passivated with 0.15%w/w BSA solution in water. The inlets of the chips were sealed with Vaseline to prevent evaporation.

The systems were recorded at 25 fps using a Pike camera (F-100B, AVT) under phase contrast illumination on a Nikon TE2000-U inverted microscope. A long-pass filter (cutoff wavelength 765 nm) was added to the optical

path to prevent phototactic response of CR and TS. The magnification was set according to the size of colloids: 30x for tracer radii of 0.5 and 1 μm, 40x for 0.25μm tracers and 20x for 1.5μm tracers.

Organisms and colloids trajectories were then digitized using a standard Matlab particle tracking algorithm (The code can be downloaded at http://people.umass.edu/kilfoil/downloads.html). Individual jumps were extracted from the trajectories with the same procedure as our previous work [48], which was completed by a visual inspection of every single events in order to filter out non-entrainment perturbations. This explains the difference between this work and the previous measurement[48] regarding the average entrainment lengths obtained with CR.

ON THE EFFECT OF FLAGELLA

To quantify the role of the flagella on the entrainment process, we first consider the impact parameter b prior an entrainment event. It has to be noted here that in the experiments we can only measure the projected impact parameter on the focal plane due to the lack of vertical resolution for both the swimmers and the colloids. However, as will be clear in what follows, this measurement allows to extract insightful information. The PDF of impact parameters b of organism-tracer encounters conditioned to the fact that the beads will be entrained PDF(b | jump) is shown Fig. 1g-main text for the three organisms after rescaling by the half-width of the organisms $w^{(\mathrm{S})}/2$ (see Fig. 1h-main text for a semi-log plot). These PDFs are akin for the three swimmers and can be well fitted by exponential distributions. However, the characteristic decay $\tilde{b}^{(\mathrm{S})} = 2b^{(\mathrm{S})}/w^{(\mathrm{S})}$ obtained for TS is larger than that of CR and OM: $\tilde{b}^{(\mathrm{TS})} = 1.0 \pm 0.3$ while $\tilde{b}^{(\mathrm{CR})} = 0.30 \pm 0.05$ and $\tilde{b}^{(\mathrm{OM})} = 0.70 \pm 0.25$, showing that TS can entrain particles even when those are relatively far away from the swimming path. We interpret this results as a consequence of the transverse gallop beating pattern of the four flagella of TS, leading to a very high probability of the beads being brought by these appendages towards the body, whatever the impact parameter, small or large. This is not true for OM and CR for which we observe more peaked distributions around $\tilde{b} = 0$, showing that particles will be entrained only if close to the swimming path. However, the distribution for CR presents a clearly visible bump above $\tilde{b} \sim 1$, also observed with other tracer sizes, Fig. 5a. This increase in the probability of entrainment at larger $\tilde{b}$ is also explained by the presence of flagella that bring the beads towards the no-slip layer of the cell. Nevertheless this effect is much less important for CR because it only has two flagella that beat synchronously.

Finally, we expect the entrainment length to decrease with impact parameter, because the larger the impact parameter b the larger the parameter ϵ_0 (Fig. 1b-main text) and consequently the further from the no-slip surface the bead will travel. To probe for this effect, we plot the entrainment length $\langle L \rangle_{b \geq a}$ averaged over impact parameters b larger than a parameter a, Fig. 5b. This reduces considerably the noise compared to simply looking at the average length at any given impact parameter. This quantity depends very weakly on a for the quadriflagellate TS, showing that the entrainment length is a weak function of impact parameters. Again this is due to the flagella bringing the beads towards the no-slip surface but in an unpredictable manner: the beads reach the no-slip surface at *random* polar angles

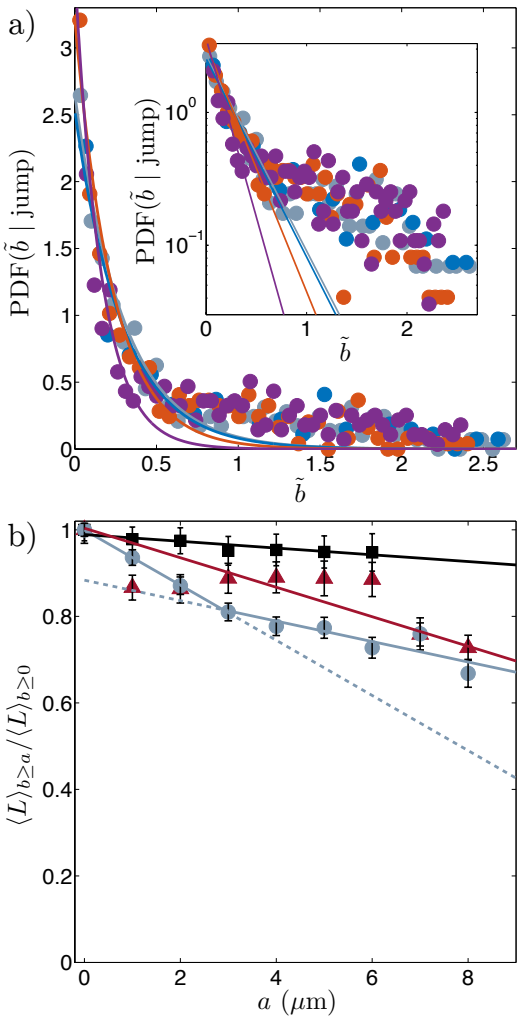

FIG. 5. (a) PDF of impact parameter b prior a jump with CR for all tracer sizes explored. All curves present a bump above $\tilde{b} \approx 1$ showing the effect of flagella bringing the tracers toward the body of the cell. Color code: blue $r_{\mathrm{P}} = 0.25\mu$m, grey $r_{\mathrm{P}} = 0.5\mu$m, orange $r_{\mathrm{P}} = 1.0\mu$m, purple $r_{\mathrm{P}} = 1.5\mu$m. Inset: Same as main curve in semi-log plot to emphasize the bumps. (b) Entrainment length averaged over impact parameters b larger than a given value a showing the effect of flagella for both TS and CR. Same color code as in main text.

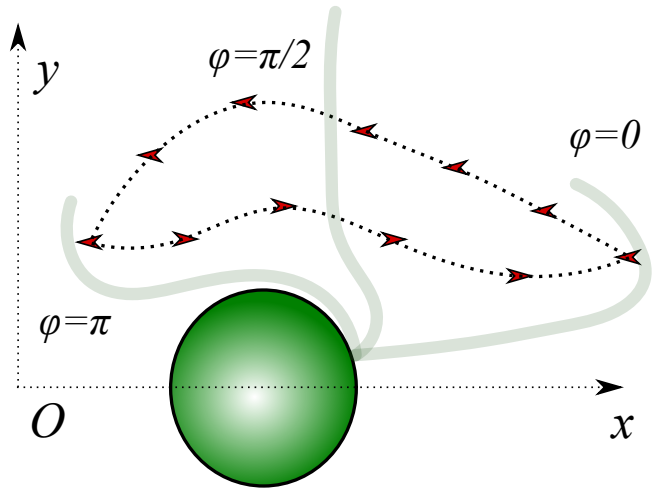

FIG. 6. Diagram of the model *Chlamydomonas* swimmer. The cell body is a sphere of radius $r_{\rm S}$ (in green) that moves along the x axis with velocity $\boldsymbol{v}_{\rm S}(\phi)$, and the flagella are represented by two point forces (red arrows) that follow a loop-like trajectory $\boldsymbol{x}_{\rm F}(\phi)$ around the cell body during the beat cycle (sketched in faint green for $\phi = 0, \pi/2, \pi$).

θ (Fig. 1b-main text) whatever the impact parameter b. For the biflagellate CR, we observe an interesting behavior where this quantity first decreases substantially up to $a \sim 3-4\ \ \mu\text{m} \sim w^{(CR)}/2$ while above the curve flattens. At small impact parameters the flagella do not play a role and the beads arrive at the surface of the cell in a more predictable way following relatively well defined pathlines. However at larger impact parameters, the flagella have an effect akin to TS and uniformise the entrainment length. For the pusher OM we seem to observe a decreasing curve with a constant slope, consistent with our interpretation of the role of the flagella with CR and TS. However the more unfrequent entrainment events for this organism limit substantially the statistics.

MODEL FOR *CHLAMYDOMONAS*

Here we present the 'outboard propulsion' model to evaluate the flow fields generated by a micro-swimmer, which we use later to perform simulations with tracer particles. We first consider a *Chlamydomonas reinhardtii* (CR) alga with a body that satisfies the no-slip boundary condition at its surface, and two beating flagella (see Fig. 6). The cell body is modelled as a solid sphere of radius $r_{\rm S}$ that is located at position $\boldsymbol{x}_{\rm S}(t) = (x_{\rm S}, 0, 0)$ at time t and oriented in the x direction, in Cartesian coordinates. The flagella are represented by two point forces (Stokeslets) that move along the trajectories $\boldsymbol{x}_{\rm F1}(\phi)$ and $\boldsymbol{x}_{\rm F2}(\phi)$ in the (x, y) plane, where both flagella exert an equal force $\boldsymbol{f}_{\rm F}(\phi)$. Here, $y_{\rm F1} = -y_{\rm F2}$ and the swimming stroke is parametrised by the beat cycle angle $\phi \in [0, 2\pi]$ with a stroke frequency of 53Hz. We assume that CR that does not rotate about the x axis, so that $\boldsymbol{f}_{\rm F}$ is purely along the x direction. This assumption can be relaxed straightforwardly.

The swimmer moves with a velocity $\boldsymbol{v}_{\rm S}(\phi)$ along the x axis, where the velocity is taken from the measurements in Ref. [4, Fig. 4b], but reduced by a factor of 0.7 to account for the confinement in our experiments. Note that the swimmer velocity oscillates throughout the stroke period, where the speed averaged over a swimming stroke is $\langle v_{\rm S}\rangle \approx 84\ \mu\text{m.s}^{-1}$. The distance progressed per stroke is $d_{\rm S} \approx 2.25\ \mu$m with a forward : backward motion ratio $\approx 3 : 0.8$.

Body flow

The Stokes solution of the flow field produced by the swimmer body that moves with a velocity $\boldsymbol{v}_{\rm S}$ through a viscous fluid, evaluated at the position $\boldsymbol{x}$ in the liquid, can be written as

$$\boldsymbol{u}_{\rm B}(\boldsymbol{r},\phi) = \frac{\boldsymbol{v}_{\rm S}}{r}\left(\frac{3r_{\rm S}}{4} + \frac{r_{\rm S}^3}{4r^2}\right) + \frac{(\boldsymbol{v}_{\rm S}\cdot\boldsymbol{r})\boldsymbol{r}}{r^2}\left(\frac{3r_{\rm S}}{4r} - \frac{3r_{\rm S}^3}{4r^3}\right), \tag{10}$$

where $\boldsymbol{r} = \boldsymbol{x} - \boldsymbol{x}_{\rm S}$ and $r = |\boldsymbol{r}|$. This solution satisfies the no-slip condition at the body's surface, $\boldsymbol{u}_{\rm B}(r = r_{\rm S}) = \boldsymbol{v}_{\rm S}$, and $\boldsymbol{u}_{\rm B} \to 0$ as $r \to \infty$. In the limit of small body sizes $r_{\rm S} \to 0$ this solution tends to the point force (Stokeslet) flow. Unless otherwise mentioned, we will use $r_{\rm S} = 3.5\ \mu$m for CR throughout this work.

Flagellar flow

The flow fields generated by the flagella must also satisfy these boundary conditions. Therefore, we model them as Stokeslets together with an image system. In the absence of a spherical surface the Stokeslet flow of the first flagellum is

$$\boldsymbol{u}_{\rm F1} = \underline{\underline{G}}(\boldsymbol{x} - \boldsymbol{x}_{\rm F1})\cdot\frac{\boldsymbol{f}_{\rm F}}{8\pi\eta}, \tag{11}$$

$$G_{ij}(\boldsymbol{r}) = \frac{\delta_{ij}}{r} + \frac{r_i r_j}{r^3}, \tag{12}$$

where G_{ij} is the Oseen tensor, η is the fluid viscosity, δ_{ij} is the Kronecker delta, and similarly for the second flagellum. The image flow field for a no-slip sphere $\boldsymbol{u}^*_{\rm F1} = \underline{\underline{G}}^*\cdot\boldsymbol{f}_{\rm F}/8\pi\eta$ is given in Ref. [78]. Together, the flagella generate the flow

$$\boldsymbol{u}_{\rm F} = \boldsymbol{u}_{\rm F1} + \boldsymbol{u}_{\rm F2} + \boldsymbol{u}^*_{\rm F1} + \boldsymbol{u}^*_{\rm F2}. \tag{13}$$

Next, the flagellar force $\boldsymbol{f}_{\rm F}$ must be related to the swimmer velocity $\boldsymbol{v}_{\rm S}$. This can be achieved by realising that the swimmer must be force free at any one time.

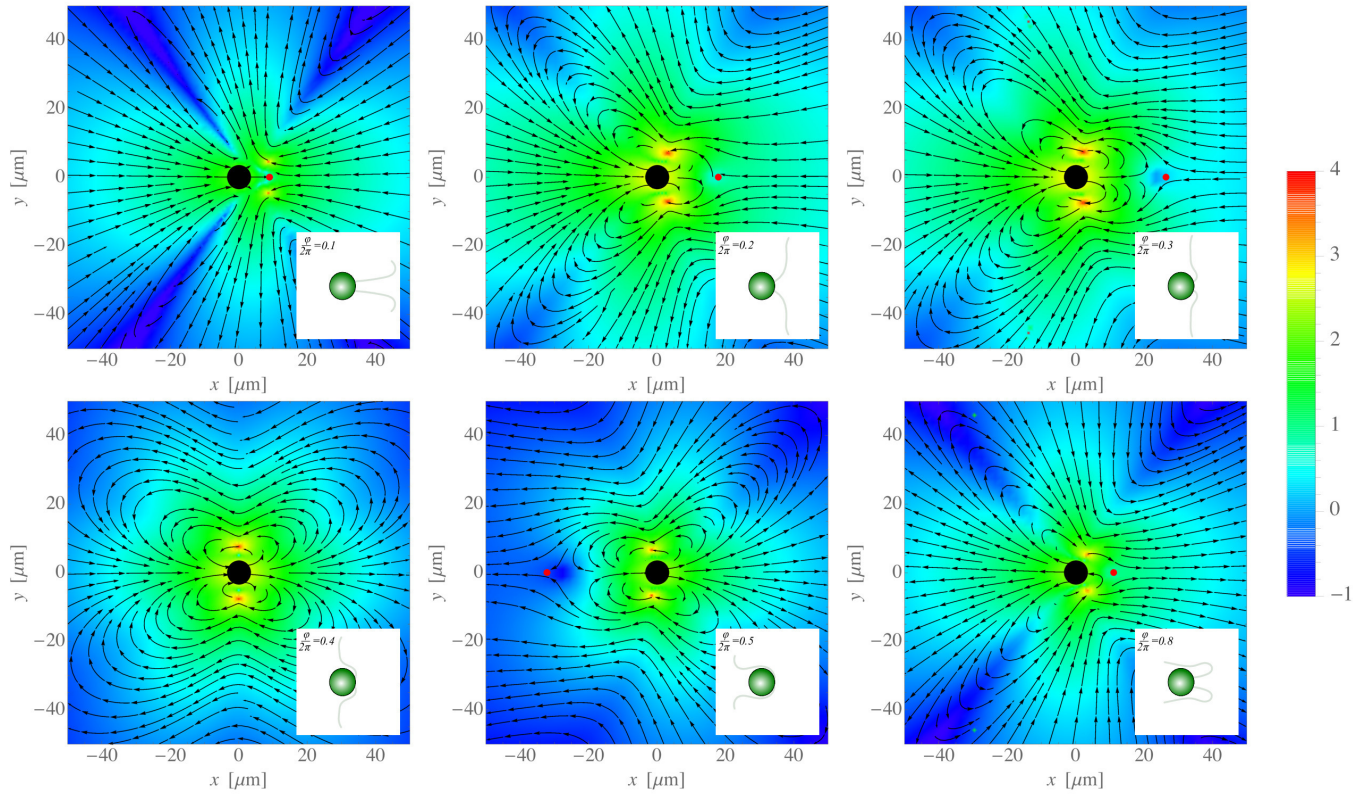

FIG. 7. Flow fields generated by the model *Chlamydomonas* , in the (x, y) plane and in the lab frame, at six different times during the swimming stroke cycle ($10\phi/2\pi = 1, 2, 3, 4, 5, 8$). The swimmer body (black disc) is oriented in the x direction, and insets show sketches of the flagellar shape at each instance. The velocity directions are shown by streamlines (black arrows) and the magnitude by colours, ranging from 10^{-1} μm.s^{-1} (blue) to 10^{4} μm.s^{-1} (red) on a logarithmic scale. The analytically approximated position (Eq. 19) of the stagnation point on the x axis is indicated with a red point.

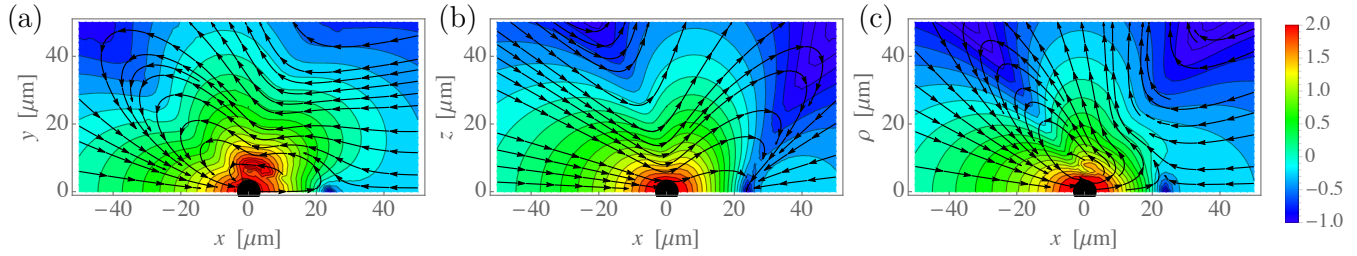

FIG. 8. Flow fields generated by the model *Chlamydomonas* in the lab frame, time-averaged over one beat cycle. (a) is the $z = 0$ cross section in which the flagella move, (b) is the $y = 0$ cross section perpendicular to the flagellar plane, and (c) shows the time- and azimuthally-averaged flow. The swimmer body (black disc) is oriented in the x direction. The velocity directions in each plane are shown by streamlines (black arrows) and the magnitude by colours, ranging from 10^{-1} μm.s^{-1} (blue) to 10^{2} μm.s^{-1} (red) on a logarithmic scale.

That is, the propulsion forces that the two flagella exert on the liquid, $2\boldsymbol{f}_{\mathrm{F,L}}$, must balance the frag force that the body exerts on the liquid, $\boldsymbol{f}_{\mathrm{B,L}}$. However, it should be noted that the flagella also exert a fraction of the force $\boldsymbol{f}_{\mathrm{F}}$ on the body, $\boldsymbol{f}_{\mathrm{F}} = \boldsymbol{f}_{\mathrm{F,L}} + \boldsymbol{f}_{\mathrm{F,B}}$, because they interact hydrodynamically. Therefore, our model swimmer must satisfy the force balance

$$\boldsymbol{f}_{\mathrm{F}} = -\tfrac{1}{2}\boldsymbol{f}_{\mathrm{B,L}} + \boldsymbol{f}_{\mathrm{F,B}}. \tag{14}$$

The drag force is known from the Stokes relation, $\boldsymbol{f}_{\mathrm{B,L}} = 6\pi\eta r_{\mathrm{S}}\boldsymbol{v}_{\mathrm{S}}$. The flagellar force on the body is evaluated by integrating the stress $\underline{\underline{\sigma}}_{\mathrm{F}}$ of the flagellar flow field over

the body's surface,

$$\boldsymbol{f}_{\mathrm{F,B}} = \oint_S \underline{\underline{\sigma}}_{\mathrm{F}} \cdot \boldsymbol{dS}, \tag{15}$$

$$\underline{\underline{\sigma}}_{\mathrm{F}} = -p_{\mathrm{F}}\underline{\underline{I}} + \eta(\nabla \boldsymbol{u}_{\mathrm{F}} + (\nabla \boldsymbol{u}_{\mathrm{F}})^T). \tag{16}$$

By evaluating this integral analytically we find that $\boldsymbol{f}_{\mathrm{F,L}} = \beta \boldsymbol{f}_{\mathrm{F}}$ and $\boldsymbol{f}_{\mathrm{F,B}} = (1-\beta)\boldsymbol{f}_{\mathrm{F}}$, where

$$\beta = 1 + \frac{r_{\mathrm{S}}^3(2\varrho_x^2 - \varrho_y^2) - 3r_{\mathrm{S}}\varrho^2(2\varrho_x^2 + \varrho_y^2)}{4\varrho^5} \tag{17}$$

depends on the relative position between the flagella and the body, $\boldsymbol{x}_{\mathrm{F}} - \boldsymbol{x}_{\mathrm{S}} = (\varrho_x, \varrho_y, 0)$, and the distance $|\boldsymbol{x}_{\mathrm{F}} - \boldsymbol{x}_{\mathrm{S}}| = \varrho$. Hence, the flagellar force can be written in terms of the swimming velocity,

$$\frac{\boldsymbol{f}_{\mathrm{F}}}{8\pi\eta} = -\frac{1}{2\beta}\frac{\boldsymbol{f}_{\mathrm{B,L}}}{8\pi\eta} = -\frac{1}{\beta}\frac{3r_{\mathrm{S}}\boldsymbol{v}_{\mathrm{S}}}{8}. \tag{18}$$

For any finite-sized body, $0 < r_{\mathrm{S}} \leq \varrho$, a finite fraction of the flagellar driving force $\boldsymbol{f}_{\mathrm{F}}$ is transferred to the body, $0 \leq \beta < 1$. In the limit $r_{\mathrm{S}} \to 0$ we recover $\beta \to 1$ so that the hydrodynamic force $\boldsymbol{f}_{\mathrm{F,B}}$ vanishes.

Note that during the simulations of tracer particles near the model swimmer, the singularities of the external Stokeslets are regularised by capping the tracer's advection speed to the organism's speed. We have tested simulations with different cut-off values and cut-off descriptions, but we observe these lead to very similar results, because the amount of time a tracer spends close to the Stokeslets is short. We do not intend to capture flagellar interactions with great accuracy in these simulations, but we aim to have a good description of the no-slip layer flows close to the body, ensuring the overall flow is force-free.

Combined swimmer flow field

Now, we can obtain the swimmer-generated flow field, $\boldsymbol{u}_{\mathrm{S}} = \boldsymbol{u}_{\mathrm{B}} + \boldsymbol{u}_{\mathrm{F}}$, by combining Eqs. 10–18 for a flagellar trajectory $\boldsymbol{x}_{\mathrm{F1}}$. To model CR we use a loop-like trajectory next to and mostly in front of the cell (Fig. 6), which is far from the body during the power stroke ($0 \leq \phi \leq \pi$) and close to the body during the recovery stroke ($\pi \leq \phi \leq 2\pi$). The resulting time-resolved flow field is shown in Fig. 7 at different times during the beat cycle. Also see Supplementary Videos 7 and 8, which show these flows in the lab frame and rest frame, respectively. This figure can be compared with the flow fields measured in experiments by Guasto *et al.* [4, Fig. 3] and Drescher *et al.* [3, Fig. 3a]. At the beginning of the power stroke (a) the flow field is almost symmetric about the y axis, and the flow strength is still weak. During the stoke however (b-c), two vortices build up diagonally behind the swimmer and the far-field flow is strongly contractile, i.e. puller-type dipole that decays as $1/r^2$ [54]. When the flagella are positioned next to the body (d) the flow is no longer dipolar, but mainly quadrupolar and decays as $1/r^3$. At the end of the power stroke (e) the swimming and flow velocities decrease, before switching sign. During the recovery stroke (f) the flagella move back towards the front of the swimmer, and the flow is moderately extensile (pusher-type) as the body moves backwards.

The position of the stagnation point, x_0 on the x axis, can be estimated analytically as a function of the flagellar position. We evaluate the flow at the point $(x_0, 0, 0)$ in the limit $r_{\mathrm{S}} \to 0$ and equate it to zero, leading to the expression

$$\frac{\varrho_y^2 + 2(x_0 - \varrho_x)^2}{\left(\varrho_y^2 + (x_0 - \varrho_x)^2\right)^{3/2}} - \frac{2}{x_0} = 0. \tag{19}$$

By solving this expression numerically, we superimpose the solution for x_0 as a red point in Fig. 7 and Video 1 throughout the beat cycle.

The beat-cycle-averaged flow fields generated by CR are shown in Fig. 8. In the xy-plane (a), there is a vortex diagonally behind the swimmer and a hyperbolic stagnation point directly in front of the swimmer at $\langle x_0 \rangle = 25\ \mu\mathrm{m} \sim 7r_{\mathrm{S}}$. In the xz-plane (b), the vortex is situated more towards the front of the swimmer but the same stagnation point features at $\langle x_0 \rangle$. The time- and azimuthally-averaged flows are shown in panel (c), which can be compared with the experimetnal measurements by Guasto *et al.* [4, Fig. 2a] and by Drescher *et al.* [3, Fig. 4a]. In all planes the swimmer is a puller in the far field, with a highly non-trivial near-field flow.

MODEL FOR *E. COLI*

Next, we focus on the *E. coli* bacterium (EC), propelled by a rotating and left-handed external helix. For simplicity we use a time-averaged model with body radius $r_{\mathrm{S}} = 0.5\ \mu$m, and the helix of length $\sim 6\ \mu$m is accounted for by N steady Stokeslets located at $\boldsymbol{x}_{\mathrm{F}i} = (-i\lambda + x_{\mathrm{S}}, 0, 0)$, where $i \in [1, \ldots N]$, $\lambda > r_{\mathrm{S}}$, and the body moves with a constant swimming speed $v_{\mathrm{S}} = 25\ \mu\mathrm{m.s}^{-1}$ along the x axis. Moreover, the body rotates with a constant angular velocity $\Omega_{\mathrm{S}} = 10\mathrm{Hz}$, and the counter rotation of the flagella is represented by four rotlets at the same positions $\boldsymbol{x}_{\mathrm{F}i}$ such that the net torque exerted on the liquid is equal to zero.

Next to the translational component from Eq. 10, the rotational flow due to the body, is

$$\boldsymbol{u}_{\mathrm{R}}(\boldsymbol{r}) = \frac{r_{\mathrm{S}}^3}{r^3}\boldsymbol{\Omega}_{\mathrm{S}} \times \boldsymbol{r}, \tag{20}$$

where $\boldsymbol{\Omega}_{\mathrm{S}} = (\Omega_{\mathrm{S}}, 0, 0)$, so that the no-slip boundary condition $\boldsymbol{u}(r = r_{\mathrm{S}}) = \boldsymbol{v}_{\mathrm{S}} + \boldsymbol{\Omega}_{\mathrm{S}} \times r_{\mathrm{S}}\hat{\boldsymbol{r}}$ is satisfied [79].

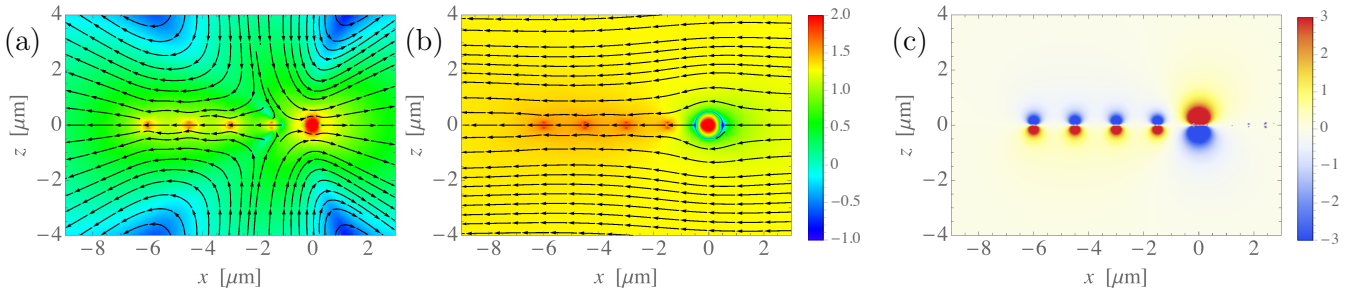

FIG. 9. Flow fields generated by the model *E. coli* bacterium, time-averaged over one helix rotation. The swimmer body is oriented in the x direction, moving with $v_S = 25\ \mu\text{m.s}^{-1}$ and rotating with $\Omega_S = 10/\text{s}$. (a) Stream lines of the radial and tangential flows in the (x, y) plane at $z = 0$, in the laboratory frame. Colours portray the flow's magnitude on a logarithmic scale, ranging from $10^{-1}\ \mu\text{m.s}^{-1}$ (blue) to $10^{2}\ \mu\text{m.s}^{-1}$ (red). (b) Same, in the co-moving frame. (c) Azimuthal flows due to the head-tail counter rotation. Colours give the magnitude of the flow's z component, on a linear scale, into the board (blue) and out of the board (red).

For the flagellar flow, using to the translational symmetry of the bacterial helix, we assume that the force and torque that each Stokeslet and Rotlet exerts is the same. However, the fraction of each force (or torque $\boldsymbol{\tau}$) exerted on the body $\boldsymbol{f}^{(i)}_{\text{F,B}}$ or liquid $\boldsymbol{f}^{(i)}_{\text{F,L}}$ is different. Hence, the flow due to the flagellum is

$$\boldsymbol{u}_{\text{F}} = \sum_{i=1}^{N} (\boldsymbol{u}_{\text{F}i} + \boldsymbol{u}^{*}_{\text{F}i}), \tag{21}$$

$$\boldsymbol{u}_{\text{F}i} = \underline{\underline{G}} \cdot \frac{\boldsymbol{f}_{\text{F}}}{8\pi\eta} + \underline{\underline{T}} \cdot \frac{\boldsymbol{\tau}_{\text{F}}}{8\pi\eta}, \quad \underline{\underline{T}} = \frac{1}{2}\boldsymbol{\nabla} \times \underline{\underline{G}}. \tag{22}$$

where, as in Eq. 13, the image system is composed of derivatives of Stokeslets and derivatives thereof. Note that the curl derivative can also be replaced by a ring of four Stokeslets around the x axis.

Now, the conditions for the swimmer to be force free and torque free are

$$0 = \sum_{i=1}^{N} \boldsymbol{f}^{(i)}_{\text{F,L}} + \boldsymbol{f}_{\text{B,L}}, \quad \boldsymbol{f}_{\text{B,L}} = 6\pi\eta r_{\text{S}} \boldsymbol{v}_{\text{S}}, \tag{23}$$

$$0 = \sum_{i=1}^{N} \boldsymbol{\tau}^{(i)}_{\text{F,L}} + \boldsymbol{\tau}_{\text{B,L}}, \quad \boldsymbol{\tau}_{\text{B,L}} = 8\pi\eta r_{\text{S}}^{3} \boldsymbol{\Omega}_{\text{S}}. \tag{24}$$

Following the derivation of Eqs. 15–18, assuming all net forces and torques are aligned with the x axis, we have the relations $\boldsymbol{f}^{(i)}_{\text{F,L}} = \beta^{(i)} \boldsymbol{f}_{\text{F}}$ and $\boldsymbol{\tau}^{(i)}_{\text{F,L}} = \gamma^{(i)} \boldsymbol{\tau}_{\text{F}}$, where

$$\beta^{(i)} = 1 + \frac{3r_{\text{S}}(i\lambda)^2 - r_{\text{S}}^3}{2(i\lambda)^3}, \tag{25}$$

$$\gamma^{(i)} = 1 + \frac{r_{\text{S}}^3}{(i\lambda)^3}. \tag{26}$$

Hence, the required Stokeslet force and rotlet torque are

$$\frac{\boldsymbol{f}_{\text{F}}}{8\pi\eta} = -\left(\sum_{i=1}^{N} \beta^{(i)}\right)^{-1} \frac{3r_{\text{S}}\boldsymbol{v}_{\text{S}}}{4}, \tag{27}$$

$$\frac{\boldsymbol{\tau}_{\text{F}}}{8\pi\eta} = -\left(\sum_{i=1}^{N} \gamma^{(i)}\right)^{-1} r_{\text{S}}^{3} \boldsymbol{\Omega}_{\text{S}}. \tag{28}$$

Finally, inserting these into Eq. 22 gives the flow due to the helix. Together with body, Eq. 10 for the translation and Eq. 20 for rotation, this completes the model for EC.

Fig. 9 shows the flow for an *E. coli* bacterium, with $N = 4$ flagellar Stokeslets and position $\lambda = 1.5\ \mu$m. In the lab frame (a), the organism clearly exhibits an extensile far-field flow – liquid is pushed out from the head and tail, and in along the waist. The origin of the dipole is located at $x \sim -2\ \mu$m, a bit closer to the body (at $x = 0$) than the flagellar tip ($x \sim -6\ \mu$m). Nearby, the liquid moves backwards parallel to the flagella but forwards with the moving body, such that the fore-aft symmetry of the dipole is broken. In the frame co-moving with the cell (b), this is emphasised as liquid flows slowly around the body and quickly past the flagella. The counter rotation of head and tail are shown in (c).

MODEL FOR *OXYRRHIS MARINA*

Lastly, we focus on the organism *Oxyrrhis marina* (OM), which is a dinoflagellate that propels by beating its posterior flagellum like a sperm cell. For simplicity, we use a time-averaged model with body radius $r_{\text{S}} = 9\ \mu$m, and the flagellum of length 48 μm is represented by four steady Stokeslets located at $\boldsymbol{x}_{\text{F}1} = (-i\lambda + x_{\text{S}}, 0, 0)$, where $i \in [1, 2, 3, 4]$, $\lambda = 12\ \mu$m, and the body moves with constant swimming speed $v_{\text{S}} = 100\ \mu\text{m.s}^{-1}$ along the x axis.

SIMULATING THE OUTBOARD MODEL

Once the flow fields $\boldsymbol{u}_{\mathrm{S}}(\boldsymbol{x},t)$ generated by each organism are known within our outboard model, we can simulate the dynamics of tracer particles. The swimmer moves with a velocity $\boldsymbol{v}_{\mathrm{S}}(t)$ along the z axis, where CR has an oscillating speed and OM and EC move with constant velocities, as described in the sections above. We assume that swimmer moves along this line for sufficiently small particles, $r_{\mathrm{P}} \lesssim r_{\mathrm{S}}$, which we observe is a reasonable assumption. This agrees with recent work by Shum and Yeomans [47], who have characterised the deflection angle of swimmers due to objects of various sizes.

For each tracer size, $r_{\mathrm{P}} = 10^{-2+3(i-1)/(8-1)}$ μm for CR and OM and $r_{\mathrm{P}} = 10^{-2+2(i-1)/(8-1)}$ μm for EC, where $i = 1, 2, ..., 7$, simulations are performed with an ensemble of $N = 10^3$ particles that do not interact with each other. Tracers are advected by the swimmer-generated velocity field with a velocity given by the Faxén relation,

$$\boldsymbol{v}(\boldsymbol{x},t) = \left(1 + \frac{1}{6}r_{\mathrm{P}}^2\nabla^2\right)\boldsymbol{u}_{\mathrm{S}}(\boldsymbol{x},t). \tag{29}$$

Particles experience steric interactions with the swimmer through a hard-core repulsion. We tried various presciptions of the repulsion potential, including the truncated Lennard-Jones (LJ) potential, $V(r) = V_{LJ}(r) - V_{LJ}(r_c) \sim r^{-12}$ with a cut-off radius $r_c \ll r_{\mathrm{P}}$, and a softer potential, $V(r) \sim r^{-6}$. To save computation time, it is also possible to set $V = 0$ and if the particle overlaps with the swimmer after a timestep, $r < r_{\mathrm{S}} + r_{\mathrm{P}}$ in the co-moving frame, renormalise the distance to $r = r_{\mathrm{S}} + r_{\mathrm{P}}$ but keep the new polar angle θ. All presciptions gave very similar results, so we used the latter method in the results presented in this work.

To simulate the Brownian motion of the tracer particles, we employ a white noise $\boldsymbol{\xi}$ defined by

$$\langle \xi_i \rangle = 0, \quad \langle \xi_i(t)\xi_j(t') \rangle = 2D\delta_{ij}\delta(t-t'), \tag{30}$$

that is drawn from a Gaussian distribution. The diffusion constant is set by the Stokes-Einstein relation,

$$D(r_{\mathrm{P}}) = \frac{k_{\mathrm{B}}\mathrm{T}}{6\pi\eta r_{\mathrm{P}}}, \tag{31}$$

where k_B is the Boltzmann constant, T is the temperature (not the contact time here), and η is the fluid viscosity.

Also see Supplementary Videos 9 and 10, which show the simulation of tracers by the outboard CR model, without Brownian noise, in the laboratory and the co-moving frame respectively. Particles are the initially arranged in equally spaced curtains, and are entrained as the swimmer passes through.

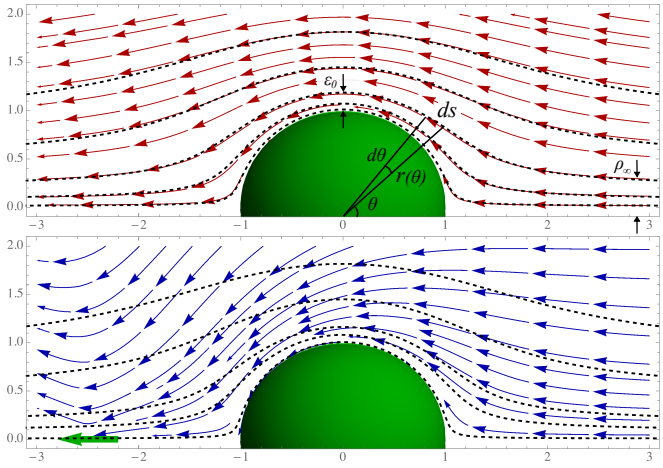

FIG. 10. Streamlines of flow fields generated by a microswimmer, in its rest frame. The organism is oriented along the positive x axis, moves with speed $v_{\mathrm{S}} = 25$ μm.s^{-1}, has a body of radius $r_{\mathrm{S}} = 1$ μm located at the origin [green sphere], and its flagella are represented by a Stokeslet located at $\lambda = 2.5$ μm and pointing in the negative x direction. Panel (a) shows the flow contribution $\boldsymbol{u}^{\mathrm{B}}$ from the swimmer body and panel (b) shows the flow $\boldsymbol{u}^{\mathrm{F}}$ due to the flagella [green arrow]. The dashed black lines are approximate stream lines from Eq. 33.

CONTACT TIME THEORY

In this section, a theoretical estimate of the contact time is obtained for a tracer particle advected by a microswimmer with a no-slip layer around its cell wall. We consider a simplified version of the 'outboard' swimmer models described above, with a spherical body of radius r_{S} and a flagella represented by only one external Stokeslet. Without loss of generality, this point force is assumed to be oriented along the negative x direction and located at a position $x = -\lambda r_{\mathrm{S}}$ with respect to the body centre for a pusher, or $x = \lambda r_{\mathrm{S}}$ for a puller, where $\lambda > 0$. This swimmer then moves with a constant velocity v_{S} along the positive x axis, and we ensure it is force-free and torque-free at all times. Hence, we examine the motion of a tracer particle in the Lagrangian frame, co-moving with the swimmer.

Stream lines

The swimmer-generated flow field is composed of two parts; the flow due to the body, $\boldsymbol{u}_{\mathrm{B}}$, and the flow due to the flagella $\boldsymbol{u}_{\mathrm{F}}$, which also contains the image system of the Stokeslet for the no-slip condition on the sphere's surface (see §). The body flow, Eq. 10, is written in spherical coordinates using the stream function

$$\psi_{\mathrm{B}}(r,\theta) = -\frac{v_{\mathrm{S}}}{2}\left(r^2 + \frac{r_{\mathrm{S}}^3}{2r} - \frac{3r_{\mathrm{S}}r}{2}\right)\sin^2\theta. \tag{32}$$

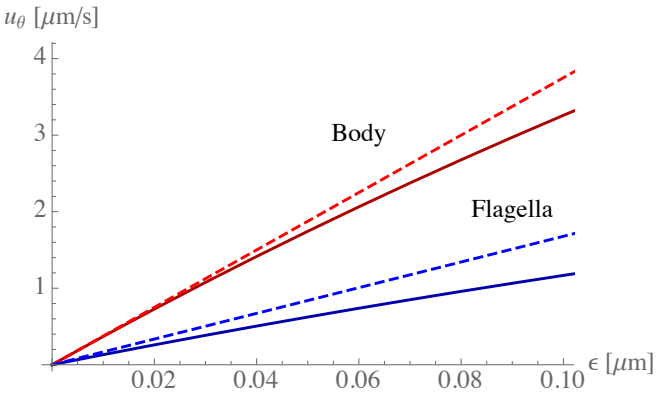

FIG. 11. Magnitude of the tangential flow along the body of a micro-swimmer, defined the same as in the caption of Fig. 10, at the equator $\theta = \pi/2$ as a function of the distance from the body ϵ. The components due to the body and flagella are shown with red lines and blue lines, respectively. Dashed lines are the linear approximations given by Eqs. 34–35.

An expression for a stream line can be obtained by equating the stream function (Eq. 32) to a constant value C_{SL}. We consider a stream line close to the swimmer body by choosing $C_{\mathrm{SL}} = -v_{\mathrm{S}} b^2/2$, where $b = \rho_\infty$ is the initial impact parameter of a tracer particle advected along that line. Solving for the radial position, we find the approximate stream line

$$r_{\mathrm{SL}}(\theta) = r_{\mathrm{S}} + \sqrt{\frac{2}{3}}\frac{b}{\sin\theta} + \mathcal{O}\left(\frac{b}{r_{\mathrm{S}}}\right)^2. \tag{33}$$

Figure 10 shows the swimmer-generated flow in its rest frame, where panel (a) only shows the flow due to the body $\boldsymbol{u}_{\mathrm{B}}$ and panel (b) shows the flow due to the flagella $\boldsymbol{u}_{\mathrm{F}}$. Note that this is a pusher-type swimmer, but the same derivation holds for pullers. For large impact parameters, $b > r_{\mathrm{S}}$, the approximation of Eq. 33 is not very good, but for stream lines close the body it is fair (Fig. 10a). Moreover, this stream line shape is also a good estimate for the flagellar flow close to the swimmer body (Fig. 10b). The closest distance of approach is given by $\epsilon_0 = b\sqrt{2/3} = r_{\mathrm{SL}}(\pi/2) - r_{\mathrm{S}}$ at the polar angle $\theta = \pi/2$.

Tangential flow near the body

The magnitude of the flow along a stream line can also be obtained by the stream function. The tangential velocity in the frame co-moving with the swimmer, $u_\theta^{\mathrm{B}} = -(r\sin\theta)^{-1}\partial\psi^{\mathrm{B}}/\partial r$, close to the swimmer body is

$$u_\theta^{\mathrm{B}}(r,\theta) = \frac{3\epsilon v_{\mathrm{S}}}{2r_{\mathrm{S}}}\sin\theta + \mathcal{O}\left(\epsilon^2\right), \tag{34}$$

where $\epsilon = r - r_{\mathrm{S}}$. The leading order of the radial component is small compared to the tangential flow, $u_r = \mathcal{O}\left(\epsilon^2\right)$. Similarly, the flagellar flow is expanded about small ϵ values to give

$$u_\theta^{\mathrm{F}} = \frac{9\lambda^3(1+\lambda)^2}{2(1+2\lambda)(1+\lambda^2)^{5/2}}\frac{\epsilon v_{\mathrm{S}}}{r_{\mathrm{S}}}\sin\theta + \mathcal{O}\left(\epsilon^2\right) \tag{35}$$

These approximations are shown in Fig. 11 with dashed lines, compared to the exact flows with solid lines, at the swimmer's equator $\theta = \pi/2$.

Note that both approximate flows satisfy the no-slip boundary condition, and grow linearly with ϵ close to the body. In the limit $\epsilon \to \infty$, the body flow u_θ^{B} tends to v_{S} in the co-moving frame and the flagellar flow u_θ^{F} decays as $1/r$. Nearby, however, the flagellar flow is of the same order of magnitude than u_θ^{B} if $\lambda \sim r_{\mathrm{S}}$, pushing or pulling liquid past the sphere. In the limit $\lambda \to \infty$, the flow u_θ^{F} decays as $1/\lambda$ and the flow generated by a colloid dragged through the liquid is recovered.

In short, the total tangential flow near the body in the co-moving frame is

$$u_\theta(r,\theta) = u_\theta^{\mathrm{B}} + u_\theta^{\mathrm{F}} \tag{36}$$

$$= \frac{3v_{\mathrm{S}}\epsilon}{2r_{\mathrm{S}}g(\lambda)}\sin\theta + \mathcal{O}\left(\epsilon^2\right), \tag{37}$$

$$g(\lambda) = \left(1 + \frac{3\lambda^3(1+\lambda)^2}{(1+2\lambda)(1+\lambda^2)^{5/2}}\right)^{-1}. \tag{38}$$

Note that for a more general flagellar orientation and position, we still expect a similar functional form of this expression with a more complex function $g(\boldsymbol{r}_{\mathrm{f}}) = (1+\tilde{g})^{-1} < 1$, because the flagella always act to push or pull the liquid past the swimmer body faster, averaged over a swimming stroke.

Contact time without noise

Our experiments show that a particle is entrained further by an organism if it spends more time near its cell wall, in the 'no-slip layer'. We compute the time taken for a particle to be advected along a stream line (Eq. 33) close to the swimmer

$$T \approx \int_{\mathrm{SL}}\frac{ds}{u_\theta} = \int_0^\pi \frac{ds}{d\theta}\frac{1}{u_\theta[r_{\mathrm{SL}}(\theta),\theta]}d\theta, \tag{39}$$

where ds is the arclength differential along the stream line parameterised by the angle $\theta \in [0,\pi]$. Inserting Eq. 33 into 37, we find that the tangential flow along a streamline is constant to first order: For a given impact parameter b we have

$$u_\theta[r_{\mathrm{SL}}(b)] = \frac{3v_{\mathrm{S}}\epsilon_0}{2r_{\mathrm{S}}}\frac{1}{g(\lambda)} + \mathcal{O}\left(\epsilon_0^2\right), \tag{40}$$

where $\epsilon_0 = b\sqrt{2/3}$ is the closest distance of approach. Therefore, taking the stream line length as the distance that a particle must travel around the swimmer, $S =$

$\int_{\mathrm{SL}} ds = \pi(r_\mathrm{S} + r_\mathrm{P})$ for small impact parameters, yields the contact time

$$T = \frac{2\pi r_\mathrm{S}(r_\mathrm{S} + r_\mathrm{P})}{3v_\mathrm{S}\epsilon_0}\, g(\lambda) \tag{41}$$

$$= \frac{\sqrt{2/3}\pi r_\mathrm{S}(r_\mathrm{S} + r_\mathrm{P})}{v_\mathrm{S} b}\, g(\lambda). \tag{42}$$

Note that in the limit of point-like tracer particles, $r_\mathrm{P} \to 0$, we recover the result by Mueller and Thiffeault [46]: The entrainment length $L = v_\mathrm{S}T = Cr_\mathrm{S}^2/b$, where the constant $C = \sqrt{2/3}\pi \sim 2.565$ for a bare no-slip sphere, as $\lambda \to \infty$ such that $g(\lambda) \to 1$, and $C < 2$ for typical swimmers. A particular feature of interest here are that the contact time, and hence the entrainment length, increases quadratically with the swimmer size r_S. This implies there is a large difference between *E. coli* bacteria and *Chlamydomonas* algae.

Finite-sized particles do not have access to the stream lines very close to the swimmer body. Therefore, if the impact parameter is so small that $0 < \epsilon_0 < r_\mathrm{P}$, these particles collide with the front of the swimmer body. Lubrication forces and steric interactions expel them, so that they cross stream lines. Hence, in the co-moving frame, they approximately move along a circular trajectory around the body when $0 < \theta < \pi/2$ and into the orbit of closest approach, the streamline with $\epsilon_0 = r_\mathrm{P}$, at $\theta = \pi/2$. As a result, the average contact time is reduced for large particles, because they cannot reach the no-slip layer close to the body and thus flow past the swimmer, as seen in its co-moving frame, more quickly.

Finally, we see that the solution diverges as $1/b$ with decreasing impact parameter. This can lead to very long entrainment events, like a ball pushed on the nose of a seal. However, this position is unstable with the introduction of thermal fluctuations, as we consider next.

Contact time with noise

We consider a Brownian particle advected in a linear shear flow over a straight solid surface that mimicks the swimmer's cell wall (main text Fig. 5a). The flow velocity is $\boldsymbol{u} = \epsilon U \boldsymbol{e}_x$, where the strain rate U derives from the velocity along a streamline, using Eq. 40, so that $U = 3v_\mathrm{S}/(2r_\mathrm{S}g(\lambda))$. A particle of radius r_P is initially positioned at $(x = 0, \epsilon = r_\mathrm{P})$, disperses with diffusivity D and is advected by the flow $\boldsymbol{u}(\epsilon)$, but cannot cross the line $\epsilon = r_\mathrm{P}$.

Without loss of generality, this system is mapped to an 'image' system (main text Fig. 5b). Here, the particle is initially located at $(x = 0, y = 0)$, the modified flow is $\boldsymbol{v} = (r_\mathrm{P} + |y|)U\boldsymbol{e}_x$, and the tracer *can* cross the surface. This is possible because the steric deflection of a particle is equivalent to the exchange of a real and an image particle, located at positions (x, y) and $(x, -y)$ respectively, with reflecting boundary conditions [66].

We aim to compute the average time $\langle T\rangle$ needed for the colloid to travel a distance $S = \pi(r_\mathrm{S} + r_\mathrm{P})$ along the positive x-direction, imitating a journey around the swimmer body. The stochastic equations of motion are

$$\dot{x}(t) = \big(r_\mathrm{P} + |y|\big)U + \xi_x(t), \quad \dot{y}(t) = \xi_y(t), \tag{43}$$

where the noise correlations are defined as

$$\langle \xi_i\rangle = 0, \quad \langle \xi_i(t)\xi_j(t')\rangle = 2D\delta_{ij}\delta(t - t'). \tag{44}$$

Note that the Faxén correction for finite-sized tracer particles need not be included here, as the Laplacian acting on pure shear flows vanishes. Integrating and averaging Eq. 43 gives

$$\langle x(t)\rangle = \int_0^t dt'\big(r_\mathrm{P} + \langle |y(t')|\rangle\big)U + \langle \xi_x(t')\rangle \tag{45}$$

$$= r_\mathrm{P}Ut + \int_0^t dt' \left\langle \left| \int_0^{t'} dt'' \xi_x(t'') \right| \right\rangle. \tag{46}$$

Using the initial condition that particles start from $y = 0$, we can employ the canonical distribution $p(y,t) = e^{-y^2/4Dt}/\sqrt{4\pi Dt}$ to give

$$\langle |y(t')|\rangle = \int_{-\infty}^{\infty} |y|\; p(y,t')dy = \sqrt{\frac{4Dt'}{\pi}}. \tag{47}$$

Inserting this expression into Eq. 45 and integrating once more then yields

$$\langle x(t)\rangle = r_\mathrm{P}Ut + \frac{4\sqrt{D}}{3\sqrt{\pi}}Ut^{3/2}. \tag{48}$$

The mean time $\langle T\rangle$ is then solution of the cubic equation

$$0 = c_0 + c_2\langle T\rangle + c_3\langle T\rangle^{3/2}, \tag{49}$$

$$c_0 = -\frac{2\pi r_\mathrm{S}(r_\mathrm{S} + r_\mathrm{P})g(\lambda)}{3v_\mathrm{S}r_\mathrm{P}};\; c_2 = 1;\; c_3 = \frac{4\sqrt{D}}{3r_\mathrm{P}\sqrt{\pi}}, \tag{50}$$

which is solved using the Cardano formula: Only one positive and real root exists for all physical situations, $c_0 < 0$ and $c_3 > 0$, which is the average contact time

$$\langle T\rangle = \left(C_+ + C_- - \frac{c_2}{3c_3}\right)^2, \tag{51}$$

$$C_\pm = \sqrt[3]{r_\mathrm{C} \pm \sqrt{q_\mathrm{C}^3 + r_\mathrm{C}^2}}, \tag{52}$$

$$q_\mathrm{C} = -\frac{c_2^2}{9c_3^2},\; r_\mathrm{C} = \frac{-27c_0c_3^2 - 2c_2^3}{54c_3^3}. \tag{53}$$

Hence, we can estimate the average entrainment length $\langle L\rangle = v_\mathrm{S}\langle T\rangle$. This analytical expression can be evaluated for different tracer sizes, swimmer speed or size, temperature, fluid viscosity, etc. Note that the theory is expected to hold best near the optimal tracer size because the approximation $\epsilon \ll r_\mathrm{S}$ in equations (33–53) holds best for particles that follow paths close to the body.

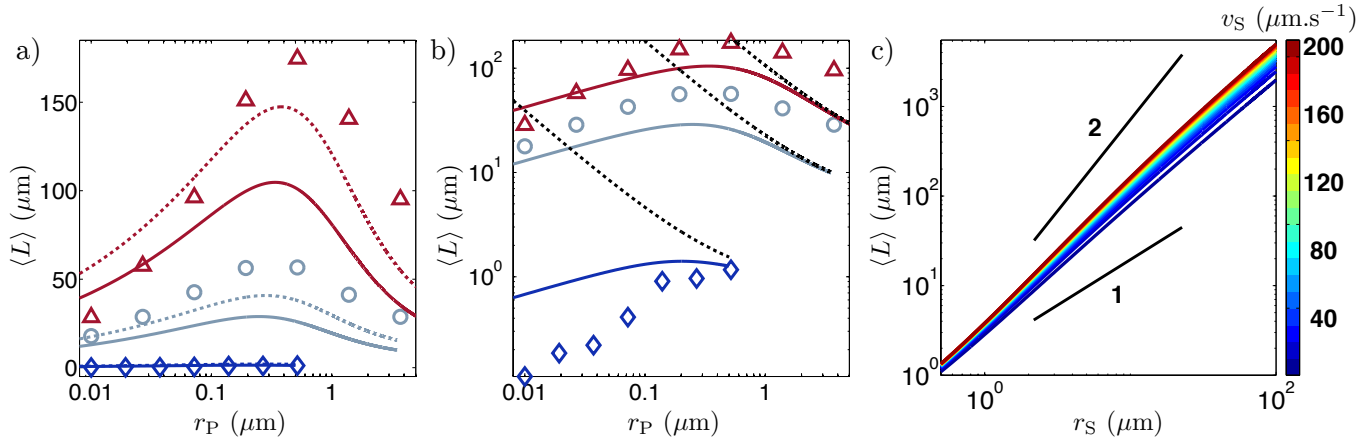

FIG. 12. a) Comparison of the entrainment lengths obtained by taking in Eq. 43 $U = \langle U(x) \rangle_x = 3v_S/(\pi r_S g(\lambda))$ (dashed lines) or $U = 3v_S/(2r_S g(\lambda))$ (full lines). The first approach gives better quantitative agreements with the numerical simulations. b) Same plot as in Fig. 3a-main text with a log-log scale. The entrainment by a bacterium (blue diamonds) never exceeds $\sim 1\mu$m because of its small size. c) Evolution of the entrainment length with the size of the organism for a fixed particle size ($r_P = 0.5\mu$m) at different velocities v_S (colorbar) and fixed $\lambda = 4$. The bigger the organism, the longer the interaction.

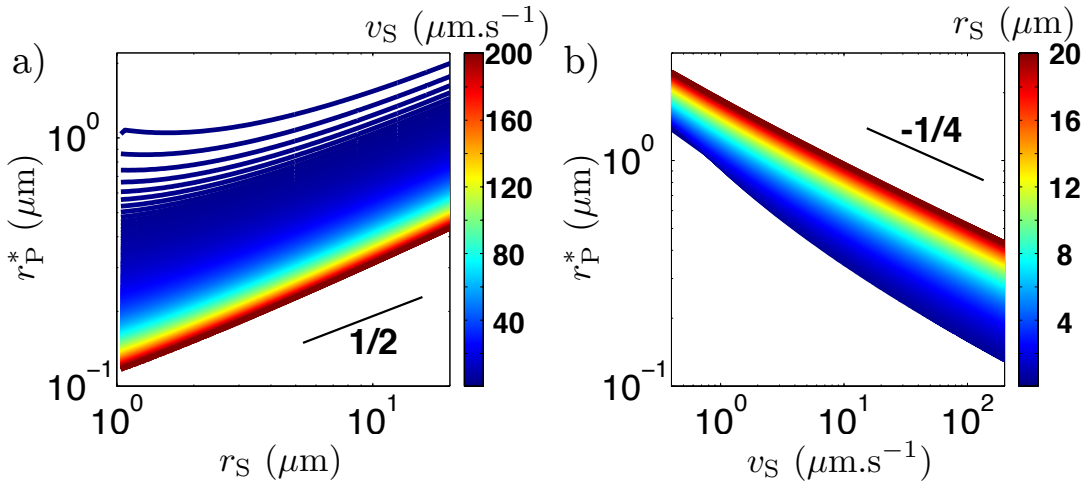

FIG. 13. a) (resp. b)) Evolution of the optimum tracer size r_P^* for entrainment with the swimmer's radius (resp. swimmer's speed) at different constant velocities (resp. radii) (colorbar) and constant $\lambda = 4$. The increase (resp. decrease) is consistent with a power law dependency with exponent 1/2 (resp. $-1/4$) as given by our simple estimate from the Péclet number (Eq. 9-main text).

Discussion

In the deterministic limit, $D \to 0$, we recover Eq. 41 immediately from Eq. 49, in agreement with Mueller and Thiffeault [46]. In this limit we do not observe a maximum in entrainment length or contact time, but a monotonic decrease with increasing particle size. This is because the smaller particles not diffuse away from small ρ values and can access the streamlines closest to the no-slip surface, whereas larger particles cannot access this region due to steric interactions and experience therefore stronger tangential flows on average.

As a consequence, large particles with small impact parameters, $b < \sqrt{3/2} r_P$ i.e. $\epsilon_0 < r_P$, can therefore not stay in their original streamline, but must *cross streamlines*. They move around the swimmer body at distance $r \approx r_P + r_S$ and polar angles $0 \lesssim \theta \lesssim \pi/2$, and subsequently move along the streamline defined by $\epsilon_0 = r_P$ at polar angles $\theta > \pi/2$ (as seen in main text Fig. 2c-d). During the first part of this trajectory, according to Eq. 37, these particles experience a tangential flow

$$u_\theta(\theta) \approx \frac{3v_S(r_P + r_S)}{2r_S g(\lambda)} \sin(\theta), \tag{54}$$

which has an explicit θ dependence, whereas the flow speed along a streamline (40) during the second part of the trajectory is approximately constant to first order. Hence, with limited diffusion, large particles might tem-

porarily be 'trapped' in the region $\theta \sim 0$ where $u_\theta(\theta) \sim \theta$. This effect is expected to *increase the contact time*, because next to the time required to flow around the body, one must add the (first-passage) time required to escape the initial low-flow region.

As a result, our simple theory *underestimates* the contact times observed in our simulations (see main text Fig. 3a). Whereas the shape of the curve and position of the maximum are captured well, we see a quantitative difference of a factor of ~ 2 near the optimal tracer size. This is expected, because the impact parameter in the stochastic model ($y(0) = 0$) is effectively equal to $b = \sqrt{3/2}r_\mathrm{P}$ rather than zero in the simulations. Indeed, by considering impact parameters in the range $b \in [0, r_\mathrm{S}]$ instead of $b = 0$ in our simulations, we retain the shape of the curve $\langle L \rangle(r_\mathrm{P})$ but the magnitude at the maximum is reduced (see main text Fig. 3b).

The current theory hinges on the simplicty of a constant flow speed along a stream line, which allows the stochastic model to be solved with an analytical expression in closed form. A more accurate approach should account for streamline crossing due to steric interactions, for example with space-dependent strain rate in Eq. 43,

$$U(x) = \frac{3v_\mathrm{S}}{2r_\mathrm{S}} \frac{1}{g(\lambda)} \sin\left(\frac{x}{r_\mathrm{S} + r_\mathrm{P}}\right), \tag{55}$$

This non-linear stochastic model is rather complex to solve mathematically and we have not yet explored it in detail. However, a way to proceed is to take the spatial average,

$$U = \langle U(x) \rangle_x = \frac{3v_\mathrm{S}}{\pi r_\mathrm{S}} \frac{1}{g(\lambda)}. \tag{56}$$

This gives a constant strain rate, so the model can be solved exactly. The resulting expression is depicted by the dashed lines in Fig. 12a. Indeed, this provides a better quantitative agreement with the outboard model simulations, especially for large particles that are subject to streamline crossing.